

Research Article www.acsami.org

Enhanced Electrochemical Performance of Rare-Earth Metal-Ion-Doped Nanocrystalline Li₄Ti₅O₁₂ Electrodes in High-Power Li-Ion **Batteries**

A. Lakshmi-Narayana, Merum Dhananjaya, Christian M. Julien, Sang Woo Joo,* and C. V. Ramana*



Cite This: ACS Appl. Mater. Interfaces 2023, 15, 20925-20945



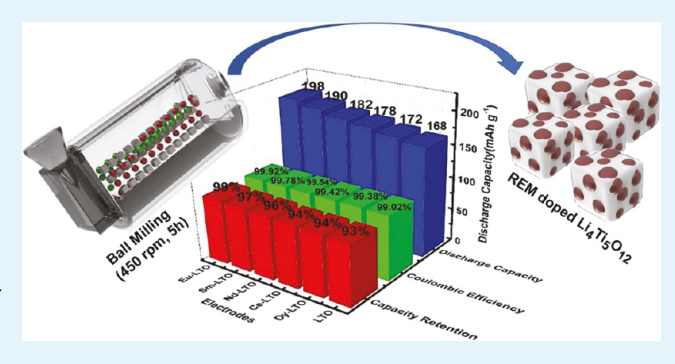
ACCESS

Metrics & More

Article Recommendations

Supporting Information

ABSTRACT: A comprehensive and comparative exploration research performed, aiming to elucidate the fundamental mechanisms of rare-earth (RE) metal-ion doping into Li₄Ti₅O₁₂ (LTO), reveals the enhanced electrochemical performance of the nanocrystalline RE-LTO electrodes in high-power Li-ion batteries. Pristi ne Li₄Ti₅O₁₂ (LTO) and rare-earth metal-doped $\text{Li}_{4-x/3}\text{Ti}_{5-2x/3}\text{Ln}_x\text{O}_{12}$ (RE-LTO with RE = Dy, Ce, Nd, Sm, and Eu; $x \approx 0.1$) nanocrystalline anode materials were synthesized using a simple mechanochemical method and subsequent calcination at 850 °C. The X-ray diffraction (XRD) patterns of pristine and RE-LTO samples exhibit predominant (111) orientation along with other characteristic peaks corresponding



to cubic spinel lattice. No evidence of RE-doping-induced changes was seen in the crystal structure and phase. The average crystallite size for pristine and RE-LTO samples varies in the range of 50-40 nm, confirming the formation of nanoscale crystalline materials and revealing the good efficiency of the ball-milling-assisted process adopted to synthesize nanoscale particles. Raman spectroscopic analyses of the chemical bonding indicate and further validate the phase structural quality in addition to corroborating with XRD data for the cubic spinel structure formation. Transmission electron microscopy (TEM) reveals that both pristine and RE-LTO particles have a similar cubic shape, but RE-LTO particles are better interconnected, which provide a high specific surface area for enhanced Li⁺-ion storage. The detailed electrochemical characterization confirms that the RE-LTO electrodes constitute promising anode materials for high-power Li-ion batteries. The RE-LTO electrodes deliver better discharge capacities (in the range of 172–198 mAh g⁻¹ at 1C rate) than virgin LTO (168 mAh g⁻¹). Among them, Eu-LTO provides the best discharge capacity of 198 mAh g⁻¹ at a 1C rate. When cycled at a high current rate of 50C, all RE-LTO electrodes show nearly 70% of their initial discharge capacities, resulting in higher rate capability than virgin LTO (63%). The results discussed in this work unfold the fundamental mechanisms of RE doping into LTO and demonstrate the enhanced electrochemical performance derived via chemical composition tailoring in RE-LTO compounds for application in high-power Li-ion batteries.

KEYWORDS: Li₄Ti₅O₁₂ (LTO), rare-earth metal, doping, Li-ion batteries, high-rate performance

INTRODUCTION

Lithium-ion batteries (LIBs) have received significant attention from the scientific and engineering community in recent years due to their efficiency as power systems for electrical vehicles (EVs), hybrid electrical vehicles (HEVs), and grid storage plants. 1-3 Continuously increasing the demand for energy and environmental problems brought on by the burning of fossil fuels made LIBs, which are known for high energy density, power density, and long shelf-life, an attractive choice. 1-3 The efficiency of a Li-ion battery mainly depends on the performance of both negative (anode) and positive (cathode) electrode materials. Most marketed LIBs are fabricated with a graphite-based anode operating at a low lithiation potential (<0.2 V vs Li⁺/Li), which causes the growth of a solid electrolyte interphase (SEI) layer deposited on the electrode surface. Lowering the available LIB capacity is due to the

irreversible expenditure of both electrons and Li⁺ ions.^{4,5} Moreover, during the charge-discharge process, the graphite anode also suffers from a volume change of 9-13%, spoiling the electrode architecture, which induces a gradual loss of interparticle electrical contact and, consequently, leading to cycle instability.^{6,7} Therefore, the development of a new anode material being an alternative to carbonaceous materials is desirable. Since the early work of Murphy et al. 8,9 studying the

Received: January 5, 2023 Accepted: March 31, 2023 Published: April 17, 2023





insertion reactions in ternary Li–Ti–O phases and that of Colbow et al. 10 evidencing the galvanostatic charge—discharge behavior of a Li//Li $_4$ Ti $_5$ O $_{12}$ cell, the spinel Li $_4$ Ti $_5$ O $_{12}$ (denoted LTO) is considered one of the most hopeful anode materials for large-scale application of Li-ion battery. Furthermore, LTO materials have the ability to be integrated with other emerging materials to form composites for application in Li-ion batteries. 11

The cubic structure of the LTO can be described using the spinel notation of $[Li_3]^{8a}[LiTi_5]^{16d}[O_{12}]^{32e}$ (or $[Li]^{8a}[Li_{1/3}Ti_{5/3}]^{16d}[O_4]^{32e}$) with the Fd3m space group. In such a network, 75% of the Li⁺ ions are located in tetrahedral 8a sites (A sites in spinel notation), whereas the 25% residual Li⁺ ions and all Ti⁴⁺ ions occupy the octahedral 16d sites (B sites), and O^{2-} anions forming a cubic-close-packed array reside in 32e sites. The three-dimensional (3D) framework of 8a-16c-8a provokes the predominant Li⁺-ion transport channel due to shortened diffusion distance and the existence of more available responsive sites. During the discharge process (intercalation), all Li ions are transferred to 16c sites and the 8a sites become empty. During charging, the deintercalation occurs as a fully reversible process with the concomitant Ti⁴⁺/ Ti³⁺ redox reaction. During charging and discharging, the 3D [LiTi₅]^{16d}[O₁₂]^{32e} spinel sublattice is extremely robust, thus showing a lattice parameter variation of less than 0.1%. 14,15 LTO exhibits a high potential of about 1.55 V vs Li⁺/Li with a plateau-like profile and ultra-long-life time without structural modification during the lithium insertion/deinsertion process. 14,16 Though LTO exhibiting a theoretical specific capacity of 175 mAh g⁻¹ is a promising anode material, its poor intrinsic transport properties, i.e., electrical conductivity of <10⁻¹⁰ S cm⁻¹ and lithium-ion diffusion coefficient of $\sim 10^{-14}$ cm² s⁻¹, have limited its practical applications.¹⁷ To overcome these issues, several strategies have been rationally employed to improve the rate performance of LTO by exploiting changes in chemical composition and/or tuning the morphology.1 Methods reported in the literature include carbon coating, 19 carbon composite, 20 nanomanufacturing, 21 morphology control,²² and elemental doping (see ref 23 and references herein).²³ Among these, elemental doping is a popular method to enhance the charge/discharge performance at high current densities. Cation or anion doping has shown the following advantages: (i) basically, LTO is an insulating material because of its empty conduction band (3d orbitals of Ti +4 state) and wide band gap,²⁴ so doping with a small amount of aliovalent cations could potentially not disrupt the basic spinel structure but could affect the local environment of ions in the lattice and bond strengths and promote the appearance of Ti³⁺ ions based on charge compensation mechanism. As doping introduces lattice defects, the concentration of electrons increases within the 3d conduction band. (ii) Doping with atoms, a larger ionic radius could potentially induce a slight lattice expansion, which might favor the Li⁺-ion diffusion pathways.²⁵

Metal-ion doping of LTO has been proven to be a helpful route not only for improving the intrinsic electronic conductivity but also for enhancing the ionic charge kinetics that typically results in high reversibility capacity and long cycle stability. Numerous studies demonstrate the substitution of various aliovalent elements on tetrahedral [Li]_{8a} sites, octahedral [Li,Ti]_{16d} sites, and [O]_{32e} sites. The common dopants located in 8a sites include Na⁺, K⁺, Mg²⁺, Ca²⁺, La³⁺, etc. Dopants in 16d sites are Fe³⁺, Al³⁺, Sc³⁺, Mo⁶⁺, Y³⁺, Nb⁵⁺, Ta⁵⁺, Zr⁴⁺, etc. Anionic dopants in 32e sites are F⁻ and Br⁻.

Note that some dopants with small ionic radii can partially occupy both Li and Ti octahedral sites such as Cr^{3+} with an ionic radius $r_i = 0.615$ Å (see the Supporting Information for more details, Table S1).

Even though the metal-ion doping in LTO is an effective strategy, only a small number of investigations have so far been documented in the literature on the electrochemical performance of lanthanide-doped LTO anodes. 26-35 Lanthanides, commonly referred to as rare-earth (RE) elements, are all transition metals sharing common properties. In their pure state, they show characteristics of brightness, metallic nature, and silvery appearance. Most of the lanthanides can be available in the stable oxidation states of +3, although +2 and +4 states are also available. In contrast, lanthanides are f-block elements because the 4f electron shell is filled. According to the literature, doping trivalent lanthanide ions (Ln3+) with a lower valence state than Ti⁴⁺ provokes oxygen vacancies in LTO, which enhance the electrochemical performance. Ln³⁺ doping elements include La³⁺, ²⁶, ²⁷ Ce⁴⁺, ²⁸, ²⁹ Sm³⁺, ³⁰ Eu³⁺, ³¹, ³² Gd³⁺, ³³, ³⁴ and Dy³⁺, ³⁵ Wu and co-workers²⁷ introduced lanthanide ions such as Gd3+ and La3+ as ionic charge carriers in the tetrahedral (8a) sites or in the octahedral sites of Ti⁴⁺ octahedral (16d) sites creating vacancies of oxygen, which could improve not only the high-rate performance but also the long-term cycling stability by enhancing electronic conductivity of the electrode. Ding et al.35 reported that sol-gelsynthesized Dy-doped LTO [Li₄Ti_{4.9}Dy_{0.06}O₁₂] delivered a high discharge capacity of 145 mAh g⁻¹ at a current rate of 0.5C with excellent cycling stability. Bai et al.²⁶ reported that the La-doped LTO (La_xLi_{4-x}Ti₅O₁₂) electrode delivered a discharge capacity of 157 mAh g^{-1} at 1C with a Coulombic efficiency close to 100% with excellent structural stability. Yang et al.³⁶ fabricated a scandium-doped LTO (Li₄Ti_{4.95}Sc_{0.05}O₁₂) using a simple solid-state reaction and showed a discharge capacity of 230 mAh g⁻¹ in the potential range of 0.0-3.0 V with excellent rate capability and structural stability. Qin et al.29 prepared Ce- and La-doped LTO electrodes, which exhibit a discharge capacity of 147 and 125 mAh g⁻¹, respectively, at a 1 A g⁻¹ current density with good cycling stability. Cai et al.³² showed that LTO doped with Eu^{2+/3+} ions $(\text{Li}_{4+x/2}\text{Ti}_{5-x/2}\text{Eu}_x\text{O}_{12}, x = 0.004)$ synthesized by a coprecipitation method delivered a discharge capacity of 199 mAh g⁻¹ at 5C rate and maintained 173 mAh g⁻¹ after long-life cycling. Li et al. 30 demonstrated that Sm-doped LTO (Li_{4-x/3}Ti_{5-2x/3}Sm_xO₁₂, x = 0.03) synthesized by solid-state reaction exhibited a discharge capacity, which exceeds 170 mAh g⁻¹ with good cycling stability. Zhou et al.³⁷ showed that, among different concentrations of cerium dopant (0.05 $\leq x \leq$ 0.2) in $\text{Li}_4\text{Ti}_{5-x}\text{Ce}_x\text{O}_{12}$, the best performance was obtained for x = 0.1. This last result prompted us to study the influence of such an RE-doping level.

In the present study, nanocrystalline LTO and rare-earth metal-doped LTO samples (Li_{4-x/3}Ti_{5-2x/3}Ln_xO₁₂ with $x \approx 0.1$ denoted hereafter as RE-LTO) were prepared through a simple mechanochemical reaction using TiO₂, LiCoO₃, and RE oxides (Dy₂O₃, CeO₂, Nd₂O₃, Sm₂O₃, and Eu₂O₃) as raw materials. The choice to use Ln³⁺ as a dopant was guided by their unique electronic properties as they have unique 4f–5d and 4f–4f electronic transitions compared to other elements that provoke oxygen vacancies in the doped LTO framework. Pure LTO and RE-LTO are studied as anode materials for Li-ion batteries. To the best of our knowledge, the effect of dysprosium and neodymium as dopants on the electrochemical performance of

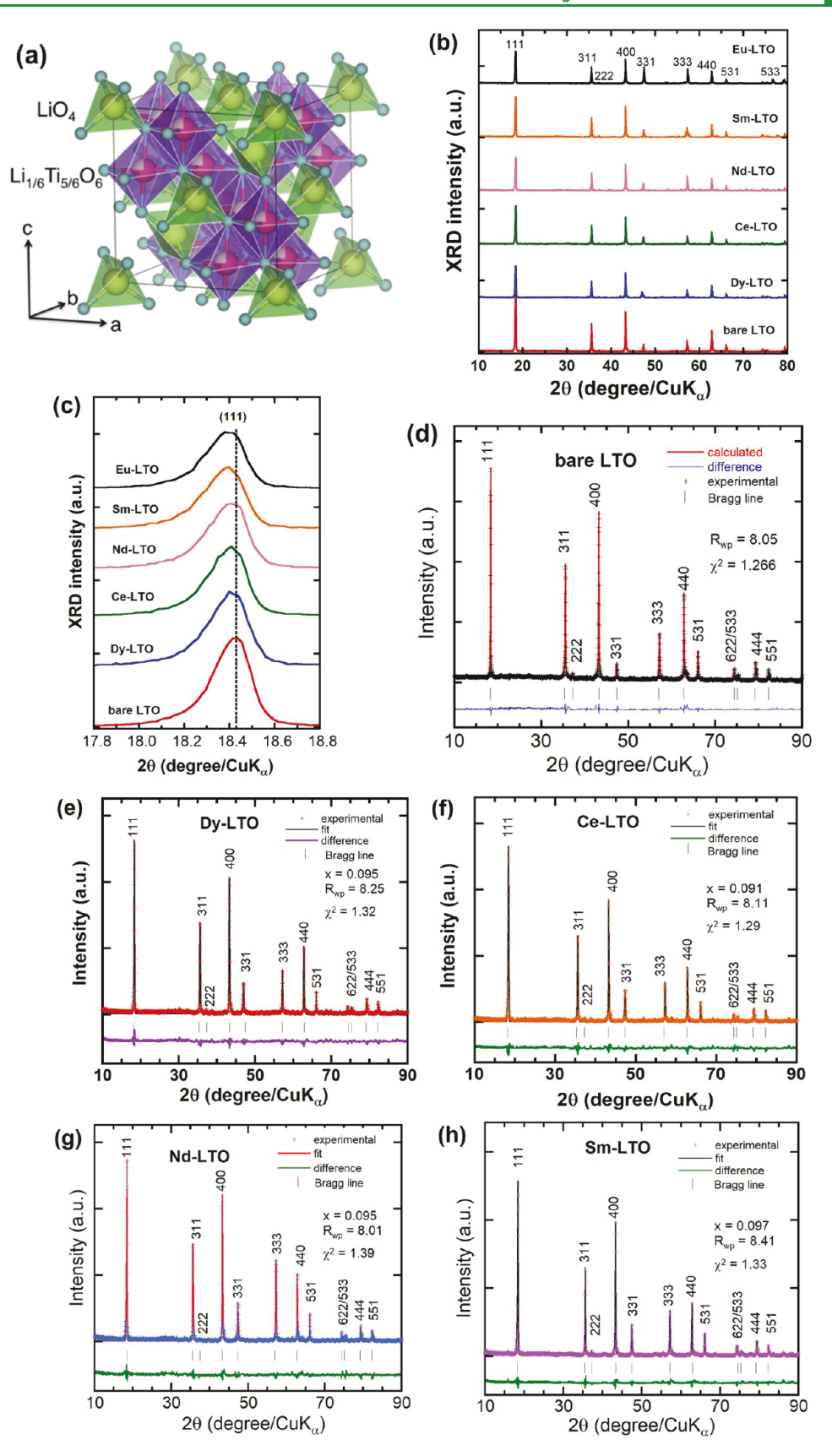


Figure 1. continued

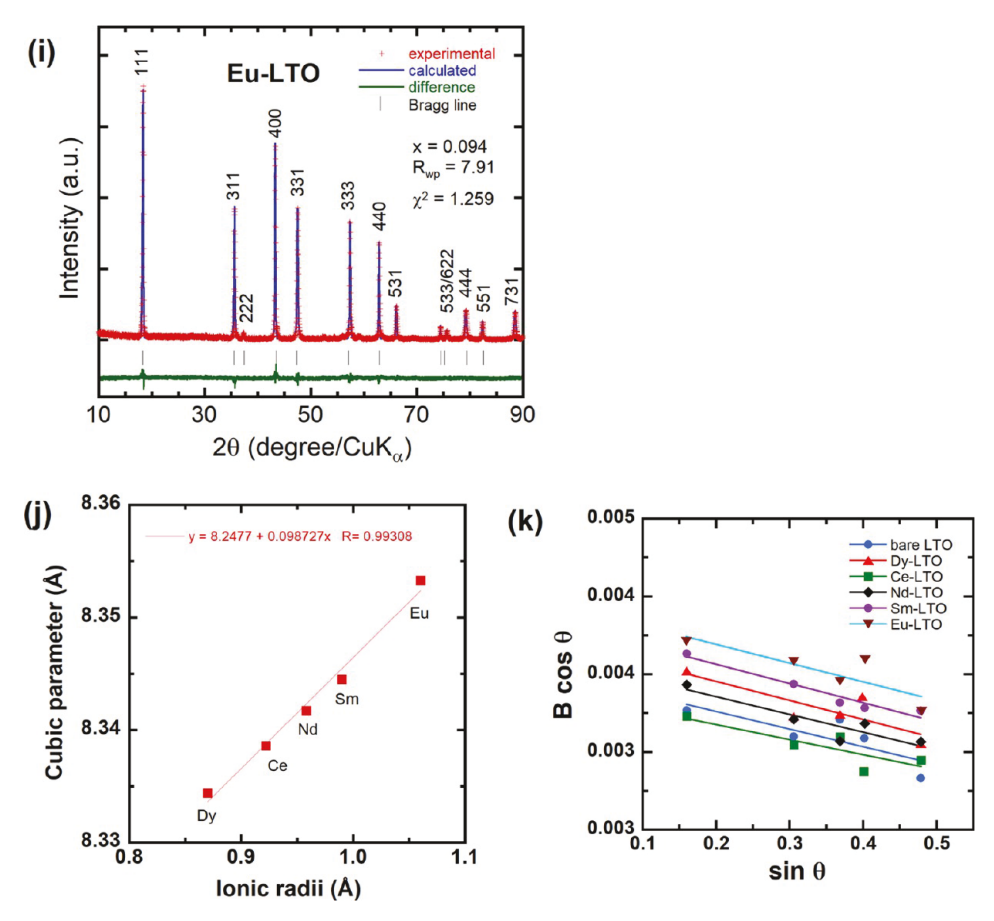


Figure 1. (a) Crystal structure of spinel Li₄Ti₅O₁₂. The tetrahedral A site is occupied by Li⁺, while the octahedral B-site is occupied by 1/6 Li⁺ and 5/6 Ti⁺⁺. Reproduced from ref 7 under the terms of the Creative Commons Attribution 4.0 International License. (b) XRD diagrams of bare LTO and RE-doped LTO nanopowders recorded using the Cu Kα X-ray source (λ = 0.15406 nm). (c) Zooming in the 2θ range 17.8–18.8° showing the (111) lattice plane region. Rietveld refinements of (d) bare LTO, (e) Dy-LTO, (f) Ce-LTO, (g) Nd-LTO, (h) Sm-LTO, and (i) Eu-LTO. (j) Lattice parameter "a" vs ionic radii of dopant elements. (k) Analysis of microstrain from the full width B at half-maximum of the XRD peaks according to eq 2.

LTO is still unknown. Moreover, there is no report comparing the electrochemical properties of Li₄Ti₅O₁₂ doped with a wide range of RE metals, such as Dy, Ce, Nd, Sm, and Eu, prepared under identical conditions, especially with the same morphology and the same grain size. Characterizations include X-ray diffraction (XRD), Raman spectroscopy, scanning electron microscopy (SEM), transmission electron microscopy (TEM), energy-dispersive X-ray analysis (EDX), Brunauer-Emmett-Teller method (BET), and X-ray photoelectron spectroscopy (XPS). The as-prepared materials were evaluated as anodes for high-power LIBs using cyclic voltammetry (CV), galvanostatic charge-discharge (GCD), cycling tests, rate capability, and electrochemical impedance spectroscopy (EIS). The Eu-doped LTO demonstrated the highest discharge capacity and highrate performance. The mechanism of the ion substitution occurring in the RE-doped LTO lattice is discussed.

EXPERIMENTAL DETAILS

Materials. All of the chemicals were purchased from Sigma-Aldrich. They were of analytical grade in good working condition and used without further purification. The chemicals used were TiO_2 (titanium(IV) oxide, anatase phase, <25 nm particle size, purity 99.7%), Li_2CO_3 (lithium carbonate, purity 99.99%), Dy_2O_3 (dysprosium(III) oxide, purity 99.9%), CeO_2 (cerium(IV) oxide, nanopowders < 50 nm particle size (BET), purity 99.5%), Nd_2O_3 (neodymium(III) oxide, nanopowders < 100 nm particle size, purity

99.9%), Sm_2O_3 (samarium(III) oxide, purity 99.9% trace metal basis), Eu_2O_3 (europium(III) oxide, purity 99.9%), and Li (lithium granular, 4–10 mesh particle size).

Synthesis of Nanocrystalline RE-LTO Electrodes. RE-LTO anode materials were prepared via a mechanochemical reaction as briefly described in the following (Figure S1). Commercial TiO₂, Li₂CoO₃, and RE metal oxides (Dy₂O₃, CeO₂, Nd₂O₃, Sm₂O₃, and Eu₂O₃) were mixed together by ball milling at a rotor speed of 450 rpm for 5 h with 0.4 mm ZrO₂ beads using ethanol as a dispersant agent. After drying at 80 °C, the mixture was calcined at 850 °C for 12 h and then grained into fine particles using an agate mortar. A 10% excess Li was used to compensate for the volatilization of Li during the calcination process at high temperature. The nominal mole ratio of RE (x = 0.1) by doping on the Ti site was maintained for all doped Li_{4-x/3}Ti_{5-2x/3}Ln_xO₁₂ samples. The pristine LTO was also synthesized using a similar process without adding RE₂O₃ oxides.

Material Characterization. Room-temperature crystallographic characteristics of as-synthesized samples were analyzed by X-ray diffraction (XRD) with a diffractometer Rigaku, model 2500PC using the Cu Kα radiation (λ = 0.15406 nm) as the X-ray source. Data were collected in the 2θ range 10–90° at a scanning rate of 0.02° min⁻¹. As-collected XRD patterns were refined using the FULLPROF software (Toolbar Fullprof suit program (3.00), version June-2015). The phase identification and morphology of the specimens were analyzed by high-resolution transmission electron microscopy (HRTEM) and selected area electron (SAE) diffraction using a HRTEM–FEI microscope (TECHNAI G2-30 S-twin D905) at an accelerating voltage of 200 kV. The surface morphology and size of

Table 1. Crystallographic Parameters of Pristine LTO and RE-LTO Powders^a

compound	$2\theta_{111}$ (degree)	$d_{111} \; (nm)$	cubic parameter (Å)	unit cell volume (\mathring{A}^3)	composition $x(RE)$	crystallite size (nm)
bare LTO	18.430	0.481(0)	8.3310	578.228		51
Dy-LTO	18.423	0.481(2)	8.3344	578.955	0.095	48
Ce-LTO	18.414	0.481(4)	8.3386	579.793	0.091	44
Nd-LTO	18.401	0.481(8)	8.3445	580.960	0.095	42
Sm-LTO	18.407	0.481(6)	8.3417	580.358	0.097	42
Eu-LTO	18.381	0.482(3)	8.3533	582.879	0.094	41

^aThe first column indicates the ionic radii of RE dopant elements. Crystallite sizes (coherent lengths) were calculated using Scherrer's formula.

the particles were investigated by field-emission scanning electron microscopy (FE-SEM) with a HITACHI S 4700 microscope. In order to enhance the conductivity of the powdered samples during the SEM measurements, an ultrathin platinum layer was deposited onto the surface of the sample by rf-sputtering (E-1030 Ion Sputter, Hitachi, Japan). The sample composition was examined using an energydispersive X-ray analysis (EDX) instrument attached to the FE-SEM apparatus. Raman scattering (RS) spectra were collected at room temperature with a confocal micro-Raman spectrometer (Horiba Jobin-Yvon HR 800 UV) using an Nd:YAG laser excitation source (λ = 532 nm) in the backscattering mode in the range of 100–900 cm⁻ at a 1 cm⁻¹ spectral resolution. A low laser power, i.e., 0.5%, 0.25 mW, was utilized to preserve the sample surface. Wavenumber calibration was performed using a silicon crystal as a reference, which displays a sharp phonon peak at 520 cm⁻¹. The N₂ adsorption-desorption isotherm measurements were carried out to determine the surface area and pore diameter/volume from an automatic surface analyzer (3-Flex, Micrometrics) using Brunauer-Emmett-Teller (BET) and Barrett-Joyner-Halenda (BJH) calculations. Morphological characterizations were acquired by the field-emission scanning electron microscope (FE-SEM) (S-4800, Hitachi, Japan). The surface properties and chemical compositions of as-prepared samples were examined by X-ray photoelectron spectroscopy (XPS) (K-alpha, Thermo Scientific) using a monochromatic Al Klpha X-ray radiation (1486.6 eV). The data were collected and processed using the marketed software Avantage (version 5.932, Thermo Scientific).

Electrochemical Characterization. The electrochemical properties of fabricated pristine LTO and RE-LTO electrodes were studied using CR2032-type coin cells. A lithium foil was utilized as the counter and reference electrodes; 1.0 mol L⁻¹ of LiPF₆ in an EC:DMC aprotic solution (1:1 ratio) was used as an electrolyte. A porous polypropylene membrane was employed as a separator. The working electrodes were fabricated by mixing the active material (80 wt %) with acetylene black (10 wt %) and poly(vinylidenefluoride) (PVDF) (10 wt %) in an N-methyl-2-pyrrolidone (NMP) solvent for 12 h. The uniformly mixed slurry was deposited onto a Cu sheet using the doctor-blade method followed by drying at 80 °C for 12 h under vacuum in a furnace before assembling the experimental cell. The mass loading of the electrodes was 2-3 mg cm⁻². The cyclic voltammetry of all prepared cells was investigated using a CHI-680C electrochemical workstation (CH Instruments Inc., Austin, Texas). The charge-discharge and cycle tests were evaluated by the multichannel battery test system (NEWARE BTS-610, MTI Corp. Richmond, California) in the voltage range from 1.0 to 2.5 V with different current densities. The room-temperature AC impedances of the cells (fully charged) were measured in the frequency range of 1 Hz to 1 MHz using the CHI-680C electrochemical workstation.

RESULTS AND DISCUSSION

Crystal Structure and Phase: XRD and Rietveld Refinement. X-ray diffraction coupled with Rietveld refinement analyses was performed to determine the structure, phase, and lattice parameters of pristine LTO and rare-earth metal-doped LTO samples, including Dy-LTO, Ce-LTO, Nd-LTO, Sm-LTO, and Eu-LTO compounds, using the $Fd\overline{3}m$ space group (spinel structure shown in Figure 1a). Figure 1b

presents the XRD data of RE-LTO samples. The appearance of the peaks and features in XRD patterns indicates that all RE-LTO compounds have similar characteristics with the basic structure of Li₄Ti₅O₁₂ spinel. In addition, no extra diffraction peaks are detectable, suggesting the high purity of the products and the successful formation of the spinel framework. The XRD LTO exhibits the predominant (111) reflection line at 2θ = 18.43° along with the other characteristic peaks (311), (400), (331), (333), (440), and (531) at $2\theta = 35.62$, 43.28, 47.40, 57.26, 62.86, and 66.09°, respectively, which correspond to the cubic spinel structure (JCPDS card no: 49-0207). The XRD pattern similarity for RE-LTO materials could be due to the synthesis procedure using ethanol as a dispersing agent, preventing the formation of TiO₂ impurities, which may arise from the crystallization of residual amorphous titania surviving the reaction.³⁹ At a relatively low concentration of RE ions substituting Ti ions, i.e., $x \approx 0.1$ in $\text{Li}_{4-x/3}\text{Ti}_{5-2x/3}\text{Ln}_x\text{O}_{12}$, the crystal structure of LTO does not change. It can be noted that the XRD patterns of the pristine LTO and RE-LTO display sharp reflection profiles, suggesting a good crystallinity of the products achieved via sintering at 850 °C for 12 h. However, it is noteworthy that a slight shift of the (111) reflection occurs toward lower 2θ angles, i.e., 18.423° for Dy, 18.414° for Ce, 18.401° for Nd, 18.407° for Sm, and 18.381° for Eu as shown by the XRD plots in Figure 1c. This shift should be attributed to the partial replacement of Ti4+ ions for RE ions in B sites of the spinel network. These results are in good agreement with previous reports in the literature. ^{27–29} To further identify the structure of RE-LTO samples, we considered their XRD Rietveld refinements as presented in Figure 1d-i. The best fits were obtained by introducing RE dopants into the octahedral 16d sites with a reliability of $R_{\rm wp} \approx 8.2$, $R_{\rm B} \approx 5.7$, and $\chi^2 \approx 1.3$. Optimized fits were also obtained by substituting three Ln3+ for every two Ti4+ and one Li+. Note that such structural refinement is able to maintain charge balance as well, indicating the stoichiometric composition $\text{Li}_{4-x/3}\text{Ti}_{5-2x/3}\text{Ln}_x\text{O}_{12}.$ All refinements were obtained considering the valence state +3 of RE dopants, except for the Eu-LTO sample, for which the best refinement was done taking the mixed oxidation state Eu²⁺/Eu³⁺ with an almost equal concentration ($x \approx 0.05$) for each species. Therefore, the introduction of RE elements into the Li₄Ti₅O₁₂ spinel phase causes a slight increase of the LTO lattice cubic parameter from a = 8.3310 Å (bare LTO) to a = 8.3344 Å (Dy-LTO) to a = 8.3533 Å (Eu-LTO). The standard deviations of these calculations were $\pm 2 \times 10^{-4}$ Å. Crystallographic parameters are listed in Table 1. As expected, the doping of LTO by the occupancy of the RE element on the Ti (16d) site causes the transition of a certain amount of Ti4+ to Ti3+ as the charge compensation results in an increase in the lattice parameter of LTO because the Ti³⁺ (0.076 nm) ionic radius is larger than that of Ti⁴⁺ (0.0605 nm). Moreover, the lattice constant and

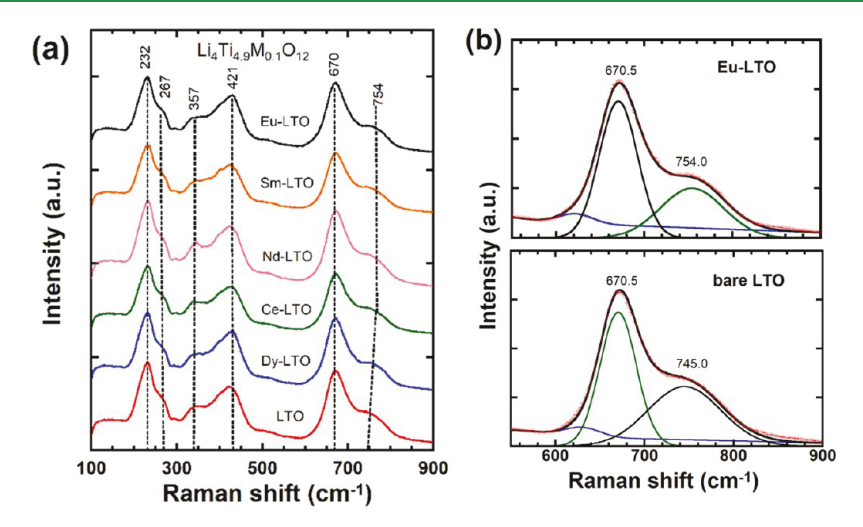


Figure 2. (a) Raman spectra recorded using the 532 nm laser line as an excitation source. (b) Zooming of the high-frequency region (550-900 cm⁻¹) with Raman band deconvolution.

unit cell volume of all doped samples increase. The increase of lattice parameters matches well with the larger ionic radii of Ln^{3+} rare-earth elements with coordination number CN = 6, i.e., $r(Dy^{3+}) = 0.0912$ nm, $r(Ce^{3+}) = 0.101$ nm, $r(Ce^{4+}) = 0.87$ nm, $r(Nd^{3+}) = 0.0983$ nm, $r(Sm^{3+}) = 0.0958$, $r(Eu^{3+}) = 0.0947$ nm, and $r(Eu^{2+}) = 0.117$ nm than that of Ti^{4+} ion $(r(Ti^{4+}) =$ 0.605 nm).40 Thus, results reveal that the RE dopants totally enter into the B-site (16d) of the spinel framework without changing the original crystal structure. Doping is expected to improve the electrochemical performance of the LTO electrode material due to the changes of lattice parameters and bond energy. Accordingly, the Eu-doped LTO sample has the highest lattice parameter and lattice volume of a =8.3533(3) Å and V = 582.879(7) Å³. Via the Rietveld analysis, the most possible composition is Li₄Ti_{4,904}Eu_{0,096}O₁₂, indicating that Eu3+ and Eu2+ ions with an average ionic radius of 0.106 nm have been successfully introduced in the lattice structure of bulk LTO. This result matches well with the work of Cai et al. 32 who reported the coexistence of Eu3+ and Eu2+ ions in Eu-doped LTO, which involves the doping into the 16d octahedral Li[‡]/Ti⁴⁺ sites of LTO, with a charge compensation $Ti^{4+} + Li^{+} = Eu^{3+} + Eu^{2+}$. Moreover, the XRD patterns of REdoped LTO show no increasing intensity of the (222) diffraction peak, demonstrating the occupation of 8a tetrahedral sites by Li rather than a heavier RE element. Consequently, LTO doped with a lanthanide element occupying the 16d site can be replicated as $Li_{4-x/2}Ti_{5-x/2}Ln_xO_{12}$.

Figure 1j depicts the relationship between the cubic parameter "a" and the six-coordinate effective ionic radii of RE dopants, confirming the successful doping process. Therefore, it is well known that the doping of LTO has several effects: (i) it causes a slight expansion of the spinel framework; (ii) the introduction of a foreign element on the Ti (16d) site can provoke the transition of a corresponding amount of Ti⁴⁺ to Ti³⁺ as a charge compensation, which also increases the lattice constant of LTO because Ti³⁺ (0.076 nm) is larger than Ti⁴⁺ (0.0605 nm). In this work, we considered that the doping rare-earth elements are located on the octahedral B sites, i.e., 16d Wyckoff sites of the spinel lattice (coordination number CN = 6) and mainly exist in the 3+ oxidation state except for Eu and Ce ions, which occur in the 3+/2+ mixed valence state as evidenced by XRD and XPS

experiments. Accordingly, the best Rietveld refinements were obtained, considering the ionic radius of the rare-earth elements with CN = 6.40 As shown in Figure 1j, the lattice parameters of the doped spinel structure follow a Vegard law with the ionic radius of dopant. The 3+ valence state of dysprosium has been previously reported by Cai et al. 41 Results of the XRD refinement are consistent with the ionic radius r_i = $0.912 \text{ Å of Dy}^{3+}$. Cerium appears with the 3+/4+ mixed oxidation state. Refinements are optimized when using the $r(\text{Ce}^{3+})/r(\text{Ce}^{4+}) = 0.87 \text{ Å ratio of } 60:40. \text{ Neodymium and}$ samarium occur only with the +3 valence state when located in the octahedral site (CN = 6); thus, $r(Nd^{3+}) = 0.983$ Å and $r(Sm^{3+}) = 0.958$ Å. Europium has been introduced into the LTO lattice with two valence states Eu^{3+} $r_i = 0.947$ Å and Eu^{2+} $r_i = 1.17 \text{ Å}$ as confirmed by XPS measurements (see below). Cai et al.³² showed that LTO doped with europium ions contains the mixed Eu^{2+/3+} valence state. In the present work, the ratio Eu^{3+}/Eu^{2+} is 1:095.

The coherent length L_c (crystallite size) of all samples was calculated using Scherrer's formula⁴²

$$L_{\rm c} = \frac{K\lambda}{\beta \cos \theta} \tag{1}$$

where θ is the diffraction angle, K is a dimensionless shape factor (0.9 for spherical-like particles), λ is the X-ray wavelength, and β is the full width at half-maximum (FWHM) of reflection lines. The average crystallite size has been estimated by considering the FWHM values of six predominant reflection peaks in the XRD patterns. The L_c values thus determined are in the range of 41-51 nm with an uncertainty of ± 1 nm (Table 1). The data (Table 1) also indicate that the nanoparticles crystallize with almost the same crystallite size and that the dopant concentration x = 0.1 does not cause modification of the strain field or stress that could disturb the grain growth process of RE-LTO. However, the diffraction peak of the (222) plane observed at ca. $2\theta = 37.25^{\circ}$ in the XRD pattern of pristine LTO is determined by the scattering power of the cations in the 8a sites. As this peak is not affected by doping, it indicates that the 8a sites are fully occupied by Li+ ions and that rare-earth metals only occupy 16d sites. Such a substitution in 16d sites provokes the partial reduction of Ti4+ to Ti3+ and induces a higher intrinsic electronic conductivity than that of pristine LTO. 43 As derived

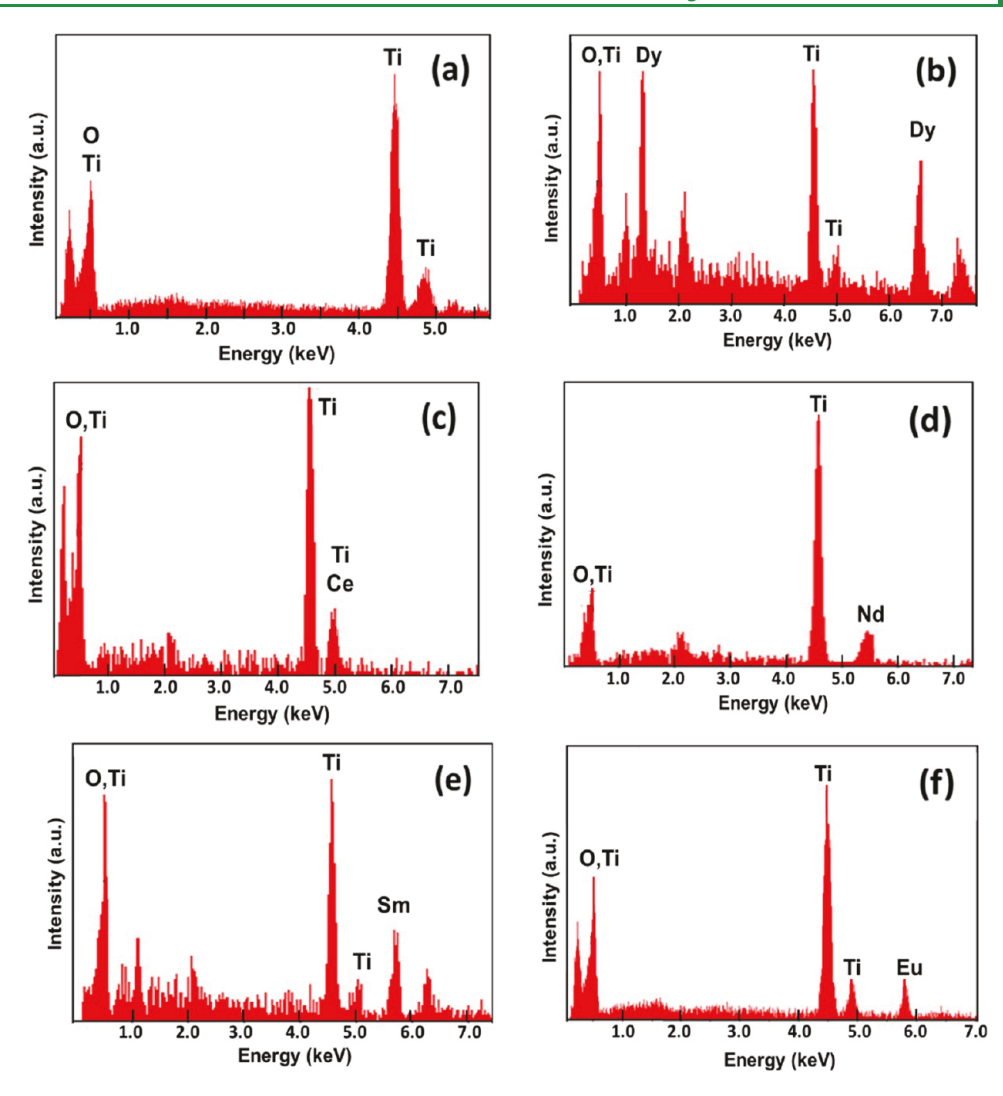


Figure 3. EDS patterns of pristine LTO (a) and RE-LTO samples: Dy-LTO (b), Ce-LTO (c), Nd-LTO (d), Sm-LTO (e), and Eu-LTO (f).

from Rietveld refinements, the LTO phase has a gravimetric density of 3.3 \pm 0.1 g cm⁻³.

Additional information on the structural properties of LTO samples such as broadening of the diffraction peaks can be a useful indicator not only for the crystallite size and crystallinity but also for the homogeneous distribution of the cations within the spinel structure. The Williamson–Hall equation was used to determine the microstrain (ε) of the particles⁴⁴

$$B_{hkl}\cos\theta_{hkl} = (K\lambda/L_c) + 4\varepsilon\sin\theta_{hkl} \tag{2}$$

where λ is the X-ray wavelength, K is the shape factor, B_{hkl} is the line broadening of a Bragg reflection (hkl), and L_c is the effective crystallite size. The microstrain is estimated from the slope of the plot $B_{hkl}\cos\theta_{hkl}$ vs $(4\sin\theta_{hkl})$, and the intersection with the vertical axis provides the crystallite size. The B_{hkl} value used here is the instrumental corrected one. From Figure 1k, the microstrain appears to be 1.1×10^{-3} rd similarly for all REdoped samples. This low value is consistent with 5.04×10^{-3} rd for LiNi_{0.5}Mn_{1.5}O₄ spinel lattices, ⁴⁵ pointing out the reduced local deformation of the structure in LTO.

Chemical Bonding: Raman Spectroscopy. Raman spectroscopy is a useful tool to probe the short-range order in solid-state materials. The Raman signal collection is

essentially from the reflection of the beam off the sample surface of compounds that strongly absorb visible light, which is the case for all electrode materials used in Li-ion batteries, i.e., carbons, silicon, transition-metal oxides, polyphosphates, etc. 46-50 Raman spectra of pristine and RE-doped LTO are presented in Figure 2a. In the spectral range of 100-900 cm⁻¹, all spectra show bands at 232, 267, 357, 421, 670, and 754 cm⁻¹. The group factor analysis, therefore, predicts five Raman-allowed phonon modes $(A_{1g} + E_g + 3F_{2g})$ for the cubic spinel $Li[Li_{1/3}Ti_{5/3}]O_4$ lattice with the $\overset{2g}{O'}_h$ factor group. All of the Raman bands present in the spectra of pristine LTO and RE-doped LTO samples confirm the spinel structure. In the Raman spectrum of Li₄Ti₅O₁₂ spinel, the Raman bands in the 700-550 cm⁻¹ region are known to be ascribable to Ti-O stretches in "TiO6" octahedra, whereas, Li being located in "LiO₄" tetrahedral, the frequencies of the Li-O stretches are known to lie within the 400-550 cm⁻¹ range. In the Raman spectrum of LTO, the strongest band at 670 cm^{-1} with a shoulder at 754 cm^{-1} is ascribed to the $A^1_{\rm lg}$ and $A^2_{\rm lg}$ Ti–O stretching vibrations in TiO_6 octahedra. The bands at 232 (F_{2g}^1) , 267 (F_{2g}^2) , and 357 (F_{2g}^3) cm⁻¹ are assigned to the bending vibrations of O-Ti-O bonds of the TiO6 octahedra, with the contribution originating from the Li-O vibrations for the band at 267 cm⁻¹ due to the partial location of Li ions in 16d sites (0.1667 occupancy). The second intensive band

located at 421 $\,\mathrm{cm}^{-1}$ is assigned to the E_g stretching vibrational mode of Li-O ionic bonds located in LiO₄ tetrahedra. ⁵⁰ A careful analysis of the high-frequency spectral range by band deconvolution (Figure 2b) shows that the Raman A_{1g} band to the Ti-O vibration has a slight red shift from 745 to 754 cm⁻¹, indicating that the doped ions successfully incorporated into the spinel LTO structure. It implies that partial doping of RE ions is doped at octahedral 16d sites occupied by Ti ions in the bare LTO. It is noticed that all Raman spectra, i.e., pristine LTO and RE-doped LTO, are similar, inferring that the quantity of RE dopant x = 0.1 does not degrade the spinel structure of LTO, which is consistent with XRD results. It should also be concluded from Raman measurements that LTO samples are free of TiO₂ anatase-like impurity, 51 which could be detected by Raman bands at 513, 403, and 143 cm⁻¹, and no traces of lanthanide oxides (Dy₂O₃, CeO₂, Nd₂O₃, Sm_2O_3 , and Eu_2O_3) are detected.

Elemental Composition: Energy-Dispersive X-ray Spectroscopy. The chemical composition of the bare and RE-doped LTO samples was characterized by energy-dispersive X-ray spectroscopy (EDS), where the energy of the X-rays emitted is the characteristic of the atom from which the emission occurs. ^{47,48} The EDS data of RE-LTO samples are presented in Figure 3a–f. The elemental analysis exhibits the O Kα and Ti Kα elemental peaks appearing at energies of 0.515 and 4.65 keV, along with the Lα characteristics of rare-earth metal dopants at 6.55, 4.97, 5.35, 5.71, and 5.81 keV for Dy, Ce, Nd, Sm, and Eu, respectively. The peak of the lithium element cannot appear in the EDS spectrum because it has a very low emission energy. ⁵² The observed atomic percentages of Ti, O, and RE elements of the RE-doped LTO are reported in Table 2. The composition of all RE-doped samples is in

Table 2. Elemental Composition (Atomic Percentage) of Pristine LTO and RE-LTO Powders

		content (atom %	5)
compound	Ti	О	RE metal
LTO	29.38	70.62	
Dy-LTO	29.06	70.50	1.74
Ce-LTO	28.64	69.89	1.75
Nd-LTO	28.90	69.96	1.34
Sm-LTO	29.33	70.90	1.77
Eu-LTO	28.98	70.66	1.46

good agreement with the nominal composition $x \approx 0.1$ obtained *via* Rietveld refinements of XRD patterns. The phase purity is evidenced by the unique fingerprint of Ti, O, and RE elements without any impurity.

Morphology and Microstructure: SEM and HRTEM. To further investigate the doping effects of RE metal ions on the phase formation and morphology of as-prepared LTO, SEM, TEM, selected area electron diffraction (SAED), and HRTEM measurements were conducted. SEM images are shown in Figure 4a–f. All samples appear as homogeneous faceted-like particles with uniformly distributed submicrometric size. It can be seen that these grains display a smooth surface with well-defined edges and corners. Note that the doping by Ln elements does not alter the particle morphology. However, after RE doping, the average particle size decreases slightly and the grains appear better interconnected. The estimated grain size for RE-doped LTO samples ($L_{\rm RE}$) decreases from \sim 120 to \sim 50 nm, in the order $L_{\rm Dy} > L_{\rm Ce} >$

 $L_{\rm Nd} > L_{\rm Sm} > L_{\rm Eu}$. The interconnected grains could be advantageous over nanosized particles, which helped to enhance electrochemical charge-transfer/Li⁺-ion storage.

The morphology and internal crystal structure of the asprepared nanopowders were further characterized by TEM, SAED, and HRTEM. Images of pristine LTO and RE-doped LTO (Dy-, Ce-, Nd-, Sm-, and Eu-LTO) are shown in Figure 5a-r, respectively. The detailed microstructure of pristine LTO shown by the low-magnification TEM bright-field image (Figure 5a) reveals the existence of well-dispersed and uniformly distributed particles with cubical shapes. The particles are in the nanoscale dimensions. Figure 5b displays SAED patterns of pristine LTO, which clearly present clear and bright spots and correspond to (111), (311), and (400) diffraction spots, indicating a high crystallinity of the material in good agreement with XRD data. These results agree well with the XRD data displayed in Figure 1. The HRTEM image (Figure 5c) confirms the well-resolved lattice of pristine LTO with fringes at an interplanar distance of 0.47 nm corresponding to the (111) plane. It can be observed that all of the bright-field low-magnification TEM images show clear cubical-shaped particles and some are interconnected with a modified shape to some extent due to the doping effect. TEM images of all RE-doped LTO samples show that particles are homogeneously distributed with an average particle size $(L_{
m TEM})$ range of 58-43 nm. Using the standard analytical procedures, 46 the average particle size was estimated from the plot of the particle size distribution (PSD) obtained from analysis of the TEM images. Graphs are shown in Figure S2, and L_{TEM} values are presented in Table S2, where the values obtained are compared with $L_{\rm c}$ values. Note that the average particle size obtained from PSD decreases from 58 to 43 nm after doping in the order $L_{\rm Dy}$ > $L_{\rm Ce}$ > $L_{\rm Nd}$ > $L_{\rm Sm}$ > $L_{\rm Eu}$, the Eu-LTO sample having the narrower PSD compared with others. It is attributed to the effect of the respective RE ion with different ionic radii, which can cause internal strain slowing down the growth of particles. The same tendency has also been observed in the XRD measurements. Minor variation in the values estimated from XRD and TEM is obvious due to the reason that the former analysis depends on several factors and statistical approaches. 46 However, while the trend of the size reduction is clear, the difference in the values is marginal from the Dy-LTO sample to the Eu-LTO sample (Table S2) due to the fact that the uncertainty for the PSD analysis is ± 3 nm. On the other hand, the XRD and TEM analyses demonstrate that the reduced crystallite size at the nanoscale ($L_c \le 50 \text{ nm}$) can be easily obtained via a mechanochemical reaction using ethanol as a dispersant agent. A significant decrease in the particle size is observed with the increase of the ionic radius of dopant. Particles for Dy-LTO and Eu-LTO have L_{TEM} values of 58 and 43 nm, respectively. Moreover, the particle distribution of the RE-doped LTO is smaller than that of pristine LTO with identical particle connection. This can be attributed to the synthesis method used and to the introduction of heterogeneous RE atoms in the host matrix, which may hinder the sintering between the primary particles. The anomalous decrease in the structural disorder of doped LTO was also revealed by Song et al.⁵³ The remarkable increase in the interatomic distance in the Ti-O bond is believed to straighten the Ti-O-Ti bond and the oxygen sublattice. The TEM images of all RE-doped LTO materials show that the primary particles are weakly interconnected and assembled into secondary particles. This weak interconnected

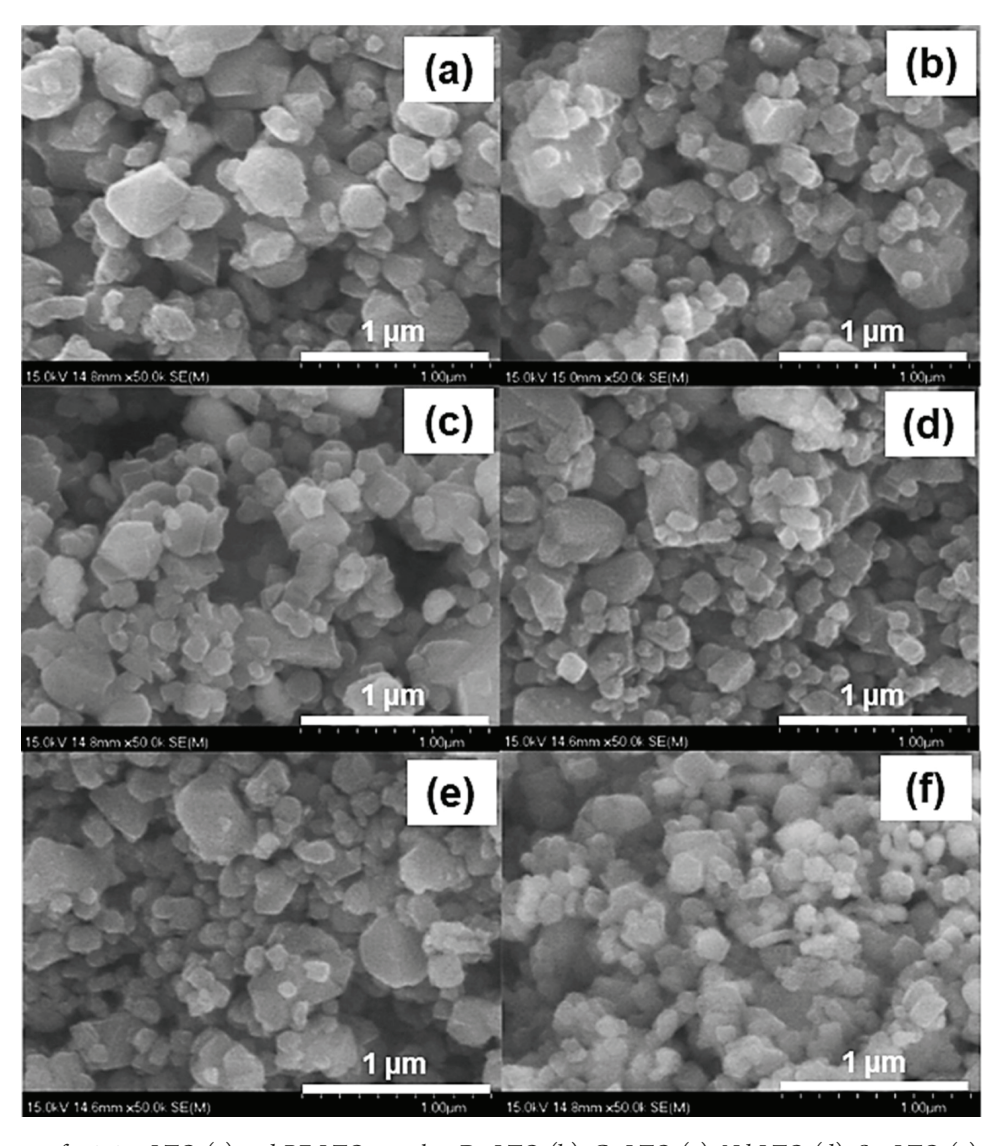


Figure 4. SEM images of pristine LTO (a) and RE-LTO samples: Dy-LTO (b), Ce-LTO (c), Nd-LTO (d), Sm-LTO (e), and Eu-LTO (f).

structure can provide additional space to store Li⁺-ion storage, which can improve the specific capacity. In addition, nanoparticles promote Li+-ion insertion/extraction due to shortened diffusion paths and the interconnected architecture at the nanoscale can guarantee the stability of the host structure.⁵⁴ With respect to HRTEM analysis, it is significant that doping can effectively limit the growth and reduce the aggregation of the submicron LTO grains. The SAED patterns of RE-doped LTO samples show a combination of bright spots, indicating that the synthesized products are well crystallized with nanoscale particles. HRTEM images presented in Figure 5 provide more detailed structural information. These images show clearly the crystalline fringes of LTO with an interplanar spacing of 0.47 nm, which agree well with the (111) planes of the spinel structure. A careful examination of HRTEM images reveals the absence of a coating layer at the particle edge, confirming the successful insertion of RE dopants into the LTO network when x = 0.1. This is unlike some literature, which reported the formation of a thin coating layer of rare-earth oxide on the grain surface.⁵⁵ From TEM images (Figure 5), one can estimate the size of primary particles, L_{TEM} , which are the assembly of crystallites. Values of L_c and L_{TEM} are listed in Table S2 for comparison.

Surface Physical Characteristics and Porosity: BET. The BET specific surface area (S_{BET}) and pore size distribution of pristine and Eu-LTO samples were determined by N2 adsorption-desorption isotherms conducted at 77 K in liquid nitrogen and are shown in Figure 6a,b. A Langmuir type-IV isotherm with a clear hysteresis loop⁵⁶ can be observed in the relative pressure (P/P_0) range of 0.6–1.0 for pristine LTO and 0.8-1.0 for Eu-LTO, which demonstrates the mesoporous (2-50 nm) nature of both samples. The adsorption increases gradually at small relative pressure for both samples, indicating the existence of the mesoporous nature. The porosity of the Eu-LTO framework appears to be higher than that of bare LTO due to the change of particle interconnection upon Eu doping. The estimated $S_{\rm BET}$ of both samples is found to be 15.67 and 30.83 m² g⁻¹, respectively. The highest surface of Eu-LTO can provide a large number of active sites caused by enhancement of the electrochemical performance. The pore size distribution of pristine LTO and Eu-LTO samples was calculated using desorption isotherm by the Barret-Joyner-Halenda (BJH) method as shown in the insets of Figure 6a,b. The average pore diameter of pristine LTO and Eu-LTO is calculated to be 17.3 and 12.5 nm with a pore volume of 0.0984 and 0.126 cm³ g⁻¹, respectively. The adsorption in the

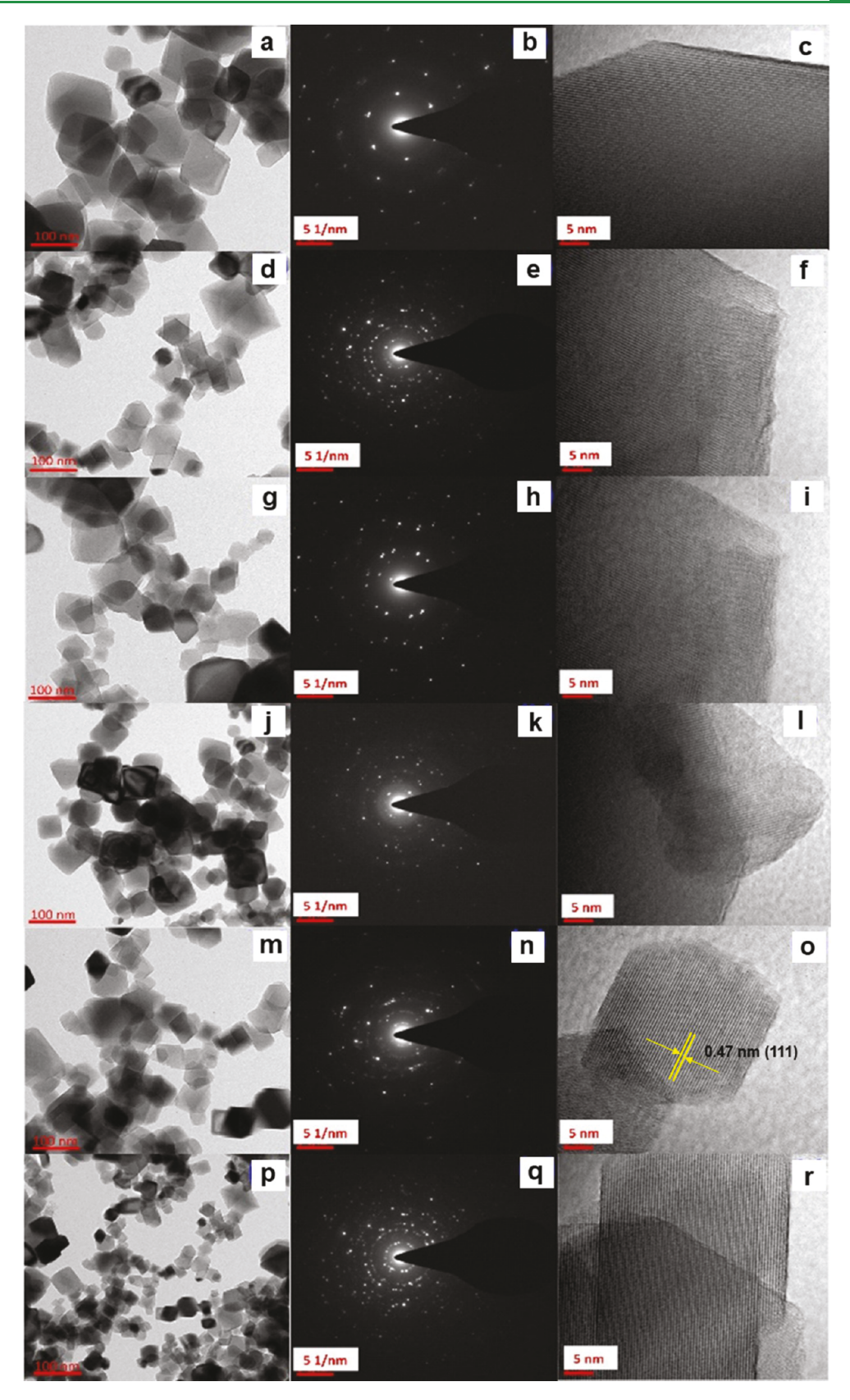


Figure 5. TEM image, SAED pattern, and HRTEM image of pristine LTO (a-c) and RE-LTO samples: Dy-LTO (d-f), Ce-LTO (g-i), Nd-LTO (j-l), Sm-LTO (m-o), and Eu-LTO (p-r). The HRTEM images show clearly the crystalline fringes of LTO with an interplanar spacing of 0.47 nm corresponding to the (111) planes of the spinel structure.

smaller relative pressure range may be related to the outer surface area of nanoparticles of both samples. The mesoporous feature, large surface area, and sufficient pore volume of both LTO and Eu-LTO samples support the conclusion that the

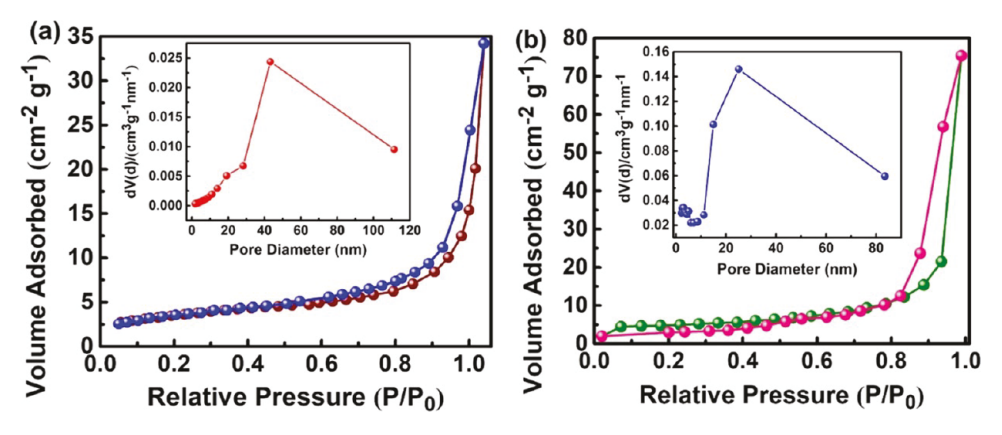


Figure 6. Nitrogen adsorption—desorption isotherms of (a) bare LTO and (b) Li₄Ti_{4.906}Eu_{0.094}O₁₂ nanopowders. The inset displays the corresponding DFT pore size distribution.

nanoscale particles not only shorten the diffusion paths for lithium ions but also provide a buffering space to accommodate the volume change during the charge—discharge process. From BET data, the equivalent particle size of samples can also be estimated and compared with values obtained from TEM images. The average diameter (in nm) of particles was calculated using the relation⁵⁷

$$L_{\rm BET} = \frac{6000}{dS_{\rm BET}} \tag{3}$$

where $S_{\rm BET}$ is the specific surface area (in m² g⁻¹) measured by BET experiments and d is the gravimetric density. Using $d=3.3~{\rm g~cm^{-3}}$ for LTO in eq 3, the $L_{\rm BET}$ results reported in Table 3 match well with the particle sizes $L_{\rm TEM}$ deduced from TEM experiments.

Table 3. BET Specific Surface Area, Pore Diameter, Pore Volume, and Calculated Average Particle Size from BET Data ($L_{\rm BET}$) Using Equation 2 and $L_{\rm TEM}$ from TEM Images

sample	$\binom{S_{\text{BET}}}{(\text{m}^2\text{ g}^{-1})}$	pore diameter (nm)	pore volume (cm³ g ⁻¹)	$L_{ m BET} \ m (nm)$	$L_{ m TEM} \ m (nm)$
bare LTO	15.67	17.3	0.0984	113	58 ± 3
Eu-LTO	30.83	12.5	0.126	57	43 ± 3

Surface Chemistry and Chemical Valence States: XPS.

The surface chemistry and oxidation states of elements of pristine LTO and Eu-doped LTO samples were assessed using X-ray photoelectron spectroscopy using a monochromatic Al $K\alpha$ X-ray radiation (1486.6 eV). Results are presented in Figure 7a-h. The survey spectra in Figure 7a validate the existence of Ti, O, and Li in bare LTO. Moreover, the element Eu is also detected in the sample Li₄Ti_{4,906}Eu_{0.094}O₁₂. Figure 7b-d shows the high-resolution XPS spectra of O 1s, Ti 3d, and Li 1s core levels for pristine LTO, respectively, while those for O 1s, Ti 3d, Li 1s, and Eu 3d of the Eu-doped LTO sample are presented in Figure 7e-h. In Figure 7b,e, both samples exhibit the typical set of the spin-orbit doublet of Ti 2p_{3/2} and Ti $2p_{1/2}$ with binding energies (BE) at 459.4 and 465.2 eV for undoped LTO and at BE of 458.4 and 464.1 eV for Eu-LTO, respectively, which matches well with the valence state +4 of Ti ions in LTO.58 Note that the BE values of doped LTO are approximately 1.0 and 1.1 lower than in bare LTO. A similar tendency has been observed for Tb³⁺-doped LTO.⁵⁹ The peak separation between these doublets ($\Delta 2p = 2p_{1/2} - 2p_{3/2}$) is 5.8

and 5.7 eV for LTO and Eu-LTO, respectively, which is also consistent with the ${\rm Ti}^{4+}$ oxidation state. In addition, the spectral deconvolution of the Ti 2p region of Eu-doped LTO (Figure 7e) reveals two components at 457.0 and 463.0 eV characteristic of Ti $2{\rm p}_{3/2}$ and Ti $2{\rm p}_{1/2}$ core level binding energies of ${\rm Ti}^{3+}$ ions. These values compared well with those of LTO materials doped with ${\rm Ce}^+$ and ${\rm Sm}^{3+}$ (Table S3). Thus, after RE doping, the ${\rm Ti}^{4+}/{\rm Ti}^{3+}$ ratio is 1:0.25, a value derived from the corresponding areas of the fitted Ti $2{\rm p}_{3/2}$ and Ti $2{\rm p}_{1/2}$ peak regions. This relative content is in good agreement with the value 22.8% after ${\rm Ce}^{3+}$ doping (x=0.15). It is well known that the reduction of ${\rm Ti}^{4+}$ ions to ${\rm Ti}^{3+}$ ones is accompanied by the creation of oxygen defects V_o - ${\rm Ti}^{3+}$ sites for charge compensation as expressed by the chemical relation referring to trivalent-ion doping ${\rm Ln}^{3+32}$

$$\operatorname{Ln}^{3+} \xrightarrow{\operatorname{doping}} \operatorname{Ln}_{\operatorname{Ti}}^{\bullet} + V_{\operatorname{O}}'' + e^{\bullet} + \frac{1}{2} \operatorname{O}_{2} (g) \tag{4}$$

$$\mathrm{Ti}^{4+} + \mathrm{e}^{\bullet} \to \mathrm{Ti}^{3+} \tag{5}$$

Based on eq 4, the substitution of Ln3+ for Ti4+ generates ${\rm Ti}^{4+}$ vacancy $({\rm Ln}_{\rm Ti}^{\bullet})$ and ${\rm O}^{2-}$ vacancy $({\it V}_{\rm O}{\it ''})$ in the LTO framework. The generated oxygen vacancy $(V_{\rm O})$ induces the partial reduction of ${\rm Ti}^{4+}$ to ${\rm Ti}^{3+}$ for charge balance (eq 5). This mechanism results in an increase of the electronic conductivity, which is mainly attributed to an increase of the electron-hole concentration. 61 In the region of the O 1s binding energies for pristine LTO (Figure 7c), the XPS band at a BE of 532.1 eV is related to the Ti-O bonding in the spinel lattice. Its counterpart in Eu-doped LTO is more complex, showing the main peak at 532.5 eV associated with a weaker band at 530.8 eV attributed to the adsorbed species such as LiOH or Li₂O on the sample surface. Figure 7d,g shows the typical peak of the Li 1s core level at BE of 54.9 and 55.3 eV for pristine LTO and Eu-LTO samples, respectively, which are values matching well with those of the literature. 62 The XPS spectra of the Eu-LTO sample (Figure 7h) show the Eu 3d core level signals observed in the BE range of 1120-1180 eV, confirming the europium doping. It can be noticed that the Eu 3d region infers the coexistence of Eu³⁺ and Eu²⁺ ions in the LTO lattice. The behavior can be attributed to the reducing atmosphere, which leads to an easy partial reduction of Eu³⁺ to Eu²⁺. The two sets of spin-orbit components $3d_{3/2}$ and $3d_{5/2}$ appear at BE of 1156.2 and 1126.5 eV for Eu²⁺ and at 1165.3 and 1134.8 eV for Eu3+, respectively. There is another evidence that a small portion of octahedral 16d Ti^{4+/}Li⁺ sites may be partial

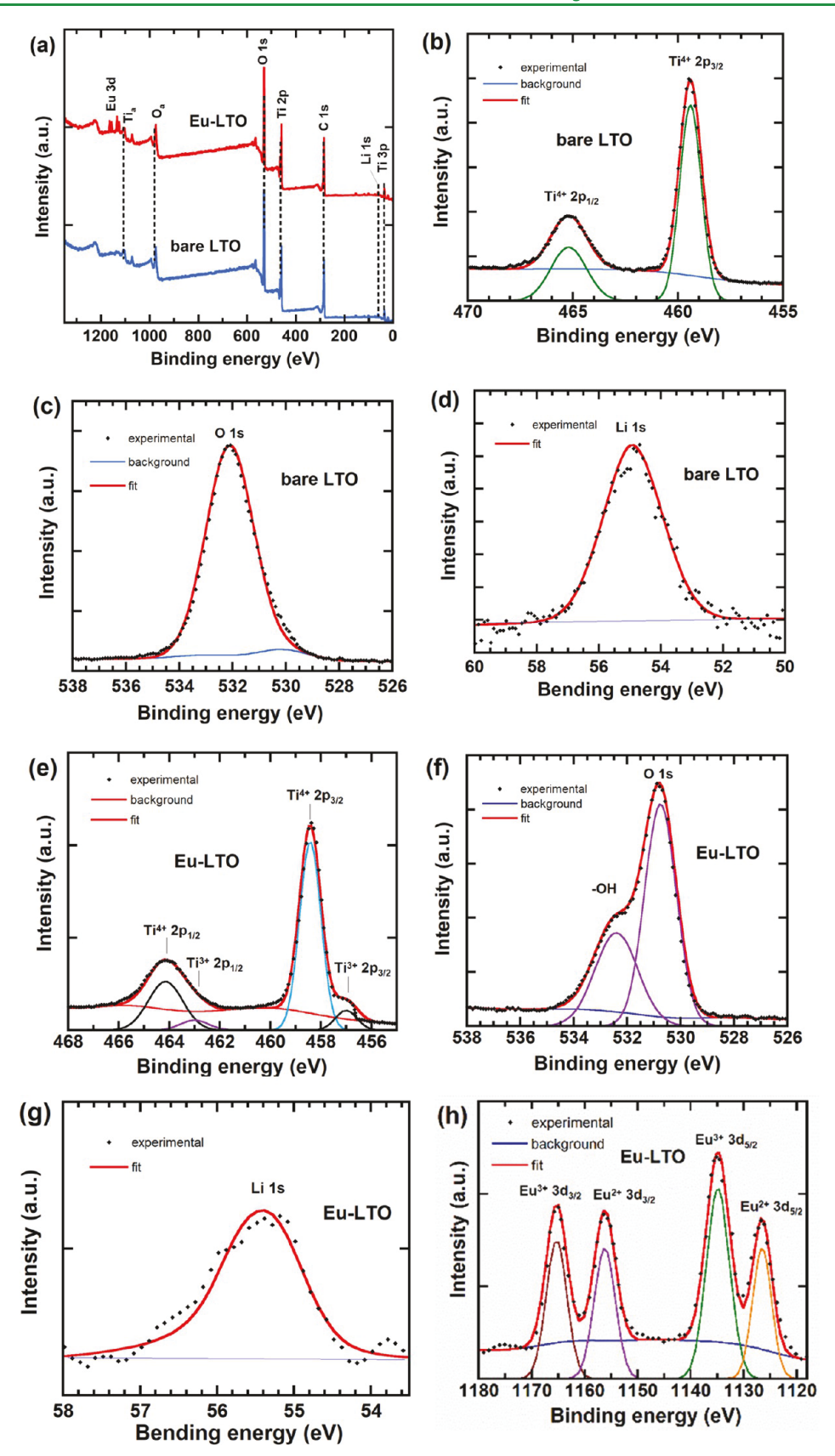


Figure 7. XPS analyses of LTO-based powders. (a) Survey spectrum of pristine LTO and Eu-LTO. (b-d) High-resolution spectra of Ti 2p, O 1s, and Li 1s for bare LTO and (e-h) high-resolution spectra of Ti 2p, O 1s, Li 1s, and Eu 3d for Eu-LTO.

reduction of Eu³⁺ to Eu²⁺ that matched well with previous reports. ^{63,64} From Figure 7h, it is also evident that the fitted

surface areas under the Eu $3d_{3/2}$ peaks are almost similar for Eu³⁺ and Eu²⁺, indicating that europium has been introduced

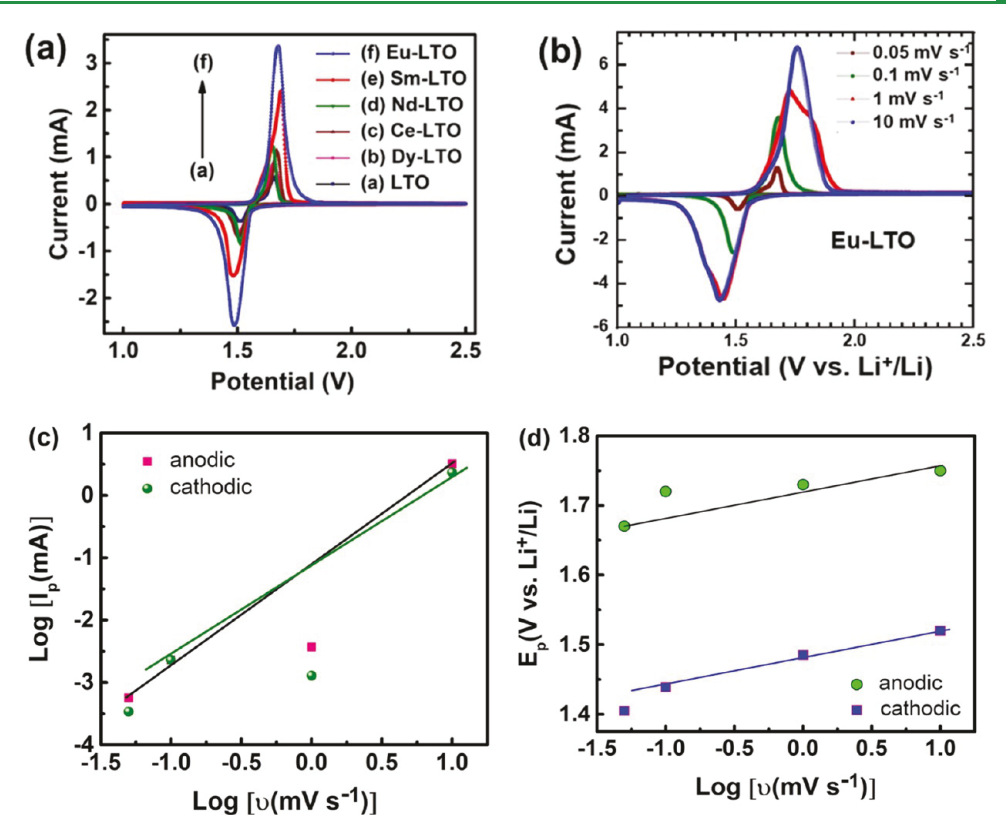


Figure 8. (a) Cyclic voltammograms of bare LTO and RE-doped LTO electrode materials recorded at a scan rate of 0.5 mV s⁻¹ in the potential range of 1.0–2.5 V vs Li⁺/Li. (b) Cyclic voltammogram of the Eu-LTO electrode recorded at different scan rates from 0.05 to 10 mV s⁻¹. (c) Log I_p vs log scan rate for the Eu-LTO electrode. (d) Potential separation $\Delta E_{\rm p} = E_{\rm pa} - E_{\rm pc}$ vs log scan rate for the Eu-LTO electrode.

in the LTO lattice with a Eu³⁺/Eu²⁺ ratio of 1:0.95, implying a valence state close to +2.5. Additionally, doping with such a mixed valence state can influence the environment of the Ti site, which results in an enhanced electron-hole concentration.

Electrochemical Properties and Performance Evaluation. The electrochemical properties and battery performance of LTO and RE-LTO electrodes were determined by lithium half-cell measurements using cyclic voltammetry (CV), galvanostatic charge-discharge (GCD), long-life cycling tests, and electrochemical impedance spectroscopy (EIS). To study the reproducibility of the electrochemical tests, several cells were tested in parallel with the same doping content. The results showed that the relative standard deviation (RSD) of the measurements was about 2%, indicating that the stability of cells was satisfactory. Kinetics of Li⁺ ions in LTO frameworks were determined via CV and EIS experiments.

Cyclic Voltammetry. Figure 8a presents the cyclic voltammetry curves of pristine LTO and RE-LTO carried out at a scan rate of 0.5 mV s⁻¹ in the potential range of 1.0-2.5 V vs Li⁺/Li. As shown in Figure 8a, the cyclic voltammograms of all electrodes have a similar narrowed sharp shape for all electrodes, indicating that the moderate amount of RE dopants ($x \approx 0.1$) does not disturb the electrochemical response of the LTO active material.³⁵ These voltammograms display one set of well-defined and redox peaks with anodic and cathodic current peaks attributed to the typical two-phase reaction of the Ti⁴⁺/Ti³⁺ redox couple corresponding to the lithium insertion/extraction in/from the LTO spinel framework,⁶⁵ and no other signals are visible. The sharper and well-defined splitting of redox peaks means that

the RE-doped LTO is well crystallized and impurity-free, which is in accordance with XRD results. Moreover, the RE doping does not affect the redox reaction nor does it modify the reversibility of the Li⁺-ion intercalation. Anodic (I_{pa}) and cathodic (I_{pc}) peaks for RE-doped LTO electrodes are more intense than that of pristine LTO, and the intensities of redox peaks for RE-LTO electrodes increase in the sequence I_{p-Dy} < $I_{
m p-Ce} < I_{
m p-Nd} < I_{
m p-Sm} < I_{
m p-Eu}$. This is the result of better reaction kinetics and lower resistance of electrodes after doping. The different peak intensities denote that RE elements are successfully doped into Ti4+ sites inducing a change in the intrinsic electrical properties of the LTO electrodes by increasing the electron-hole concentration. Individual normalized voltammograms in Figure S3 and data listed in Table 4 show that the anodic and cathodic peak potentials E_{pa}/E_{pc} vs Li^+/Li are observed in the range of 1.66–1.69 and 1.48–1.53

Table 4. Cyclic Voltammetry Results for Pristine LTO and RE-Doped LTO Electrodes

electrode	anodic $E_{\rm pa}$ (V)	cathodic $E_{\rm pc}$ (V)	$\frac{\Delta E_{\rm p}}{({ m V})}$	$(\mathrm{cm}^2 \mathrm{s}^{-1})$	$D_{\mathrm{Li-ox}^+\atop (\mathrm{cm}^2\mathrm{s}^{-1})}$
LTO	1.69	1.48	0.21	5.0×10^{-13}	5.4×10^{-13}
Dy-LTO	1.67	1.49	0.18	5.6×10^{-12}	7.7×10^{-12}
Ce-LTO	1.67	1.51	0.16	7.1×10^{-12}	8.3×10^{-12}
Nd-LTO	1.67	1.52	0.15	9.7×10^{-12}	8.8×10^{-12}
Sm-LTO	1.66	1.52	0.14	1.1×10^{-11}	9.4×10^{-12}
Eu-LTO	1.66	1.53	0.13	2.8×10^{-11}	1.1×10^{-11}

^aAnodic $E_{\rm pa}$ and cathodic $E_{\rm pc}$ potentials, potential differences $\Delta E_{\rm p}$ measured at a scan rate of 0.5 mV s⁻¹, and Li-ion diffusion coefficients of reduction $(D_{Li^+}\text{-red})$ and oxidation $(D_{Li^+}\text{-ox})$ processes.

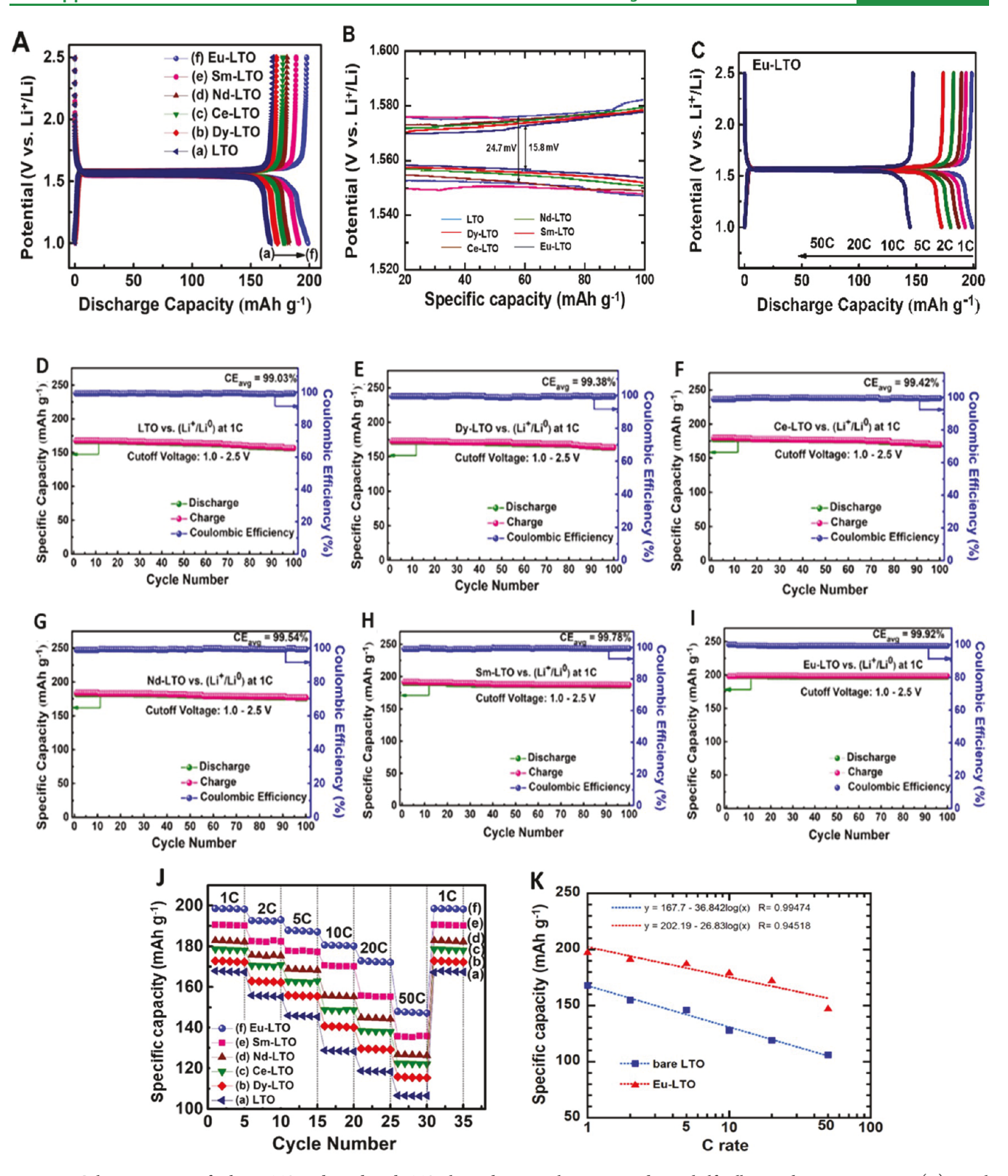


Figure 9. Galvanostatic tests for bare LTO and RE-doped LTO electrode materials investigated in Li half-cells at ambient temperature. (A) Initial galvanostatic charge—discharge profiles recorded at 1C rate in the potential range of 1.0–2.5 V vs Li⁺/Li. (B) Magnification of the GCD profiles showing the electrode polarization phenomena in the potential between 1.525 and 1.600 V. (C) GCD profiles of the EU-LTO electrode cycled at various C-rates. (D–I) Specific discharge capacity and Coulombic efficiency vs cycle number of electrodes tested at 1C rate. (D) Bare LTO, (E) Dy-LTO, (F) Ce-LTO, (G) Nd-LTO, (H) Sm-LTO, and (I) Eu-LTO. (J) Rate capability of bare LTO and RE-LTO electrodes tested from 1C to 50C rate. (K) Modified Peukert plots for LTO and Eu-LTO electrodes tested in the potential range of 1.0–2.5 V vs Li⁺/Li.

V, respectively. Generally, the potential separation $\Delta E_{\rm p} = E_{\rm pa} - E_{\rm pc}$ between the anodic and cathodic peak currents in the CV

curves reflects the degree of polarization of the electrode. As shown in Figure 8a, ΔE_p varies from 0.21 V in bare LTO to

0.13 V in Eu-LTO in the order $\Delta E_{\text{p-LTO}} > \Delta E_{\text{p-Dy-LTO}} >$ $\Delta E_{\text{p-Ce-LTO}} > \Delta E_{\text{p-Nd-LTO}} > \Delta E_{\text{p-Sm-LTO}} > \Delta E_{\text{p-Eu-LTO}}$, indicating the decreasing degree of polarization of the RE-doped electrodes due to the higher electrical conductivity that can be associated with the influence of particle size and inherent properties of electrode materials after doping, i.e., interactions between electronic states of Ti and RE dopants. Thus, the results and CV characterization indicate faster kinetics for the RE-doped electrodes. As expected, when RE ions enter the LTO lattice, the slight increase of the elementary cell volume induces an expansion of the channels for Li-ion insertion and extraction, which improves the rate performance of LTO.

The high-rate performance of Li//LTO half-cells significantly depends on their kinetic origin, which was investigated by CV characterizations in detail. Figure 8b presents the CV curves of the Li//Eu-LTO half-cell at varied scan rates from 0.05 to 10 mV s^{-1} in a voltage window from 1.0 to 2.5 V(Figure S4). The peak currents (I_p) and scan rates (ν) have a relationship expressed by eq 660

$$I_{p} = \alpha \ \nu^{\beta} \tag{6}$$

which can be rewritten as

$$\log(I_{\rm p}) = \beta \log(\nu) + \log(\alpha) \tag{7}$$

where β represents the slope of $\log(I_{\rm p})$ $\nu s \log(\nu)$ curve, being often in a range of 0.5-1. The electrochemical reaction is controlled by ionic diffusion when $\beta = 0.5$, while a pseudocapacitance behavior dominates the charge/discharge process when $\beta = 1$. By fitting the plots of $\log(I_p)$ vs $\log(\nu)$ (Figure 8c), the calculated β values of anodic and cathodic peaks are 0.48 and 0.51, respectively, suggesting that the electrochemical reaction of Li//LTO cells is a pure diffusioncontrolled mechanism. This characteristic is believed to be responsible for the high-rate performance of LTO as the RE doping in the LTO crystal lattice can effectively increase the intrinsic electronic conductivity or Li⁺-ion diffusion. However, as shown in Figure 8c, Li⁺-ion transport across the LTO network is faster during the oxidation (anodic) reaction than during reduction (cathodic) due to the occurrence of the twophase mechanism and poor ionic conductivity of the fully reduced Li₇Ti₅O₁₂ phase. This phenomenon corresponds to higher apparent chemical diffusion coefficients for the oxidation process (Table 4). Another interesting characteristic of LTO materials can be viewed by the plot of the peak potential E_p vs $\log(\nu)$ as shown in Figure 8d. Due to electrode polarization, an increasing scan rate results in a higher peak current and increased anodic/cathodic peak separation. Moreover, the peak potentials correlate well with $log(\nu)$ and resulted in a straight line, allowing for the estimation of redox reversibility for the RE-doped LTO electrodes.

The apparent chemical diffusion coefficients, D_{Li} , of Li ions into bare LTO and RE-doped LTO frameworks were calculated using the Randles-Sevick equation 69

$$i_{\rm p} = kn^{3/2}AC_0D_{\rm Li}^{1/2}v^{1/2} \tag{8}$$

where i_p is the anodic peak current (A) from CV plots, k = 2.69 \times 10⁵ is the constant expressed in C mol⁻¹ V^{-1/2}, A is the effective surface area of the anode (cm^2) , n is the number of electrons for Li⁺ transferred, C_o is the molar concentration of Li ions in LTO (4.37 \times 10⁻³ mol cm⁻³), $D_{\rm Li}$ is the chemical diffusion coefficient of Li ions, and ν is the scan rate (0.05 mV s⁻¹). By using eq 8 and equations obtained from linear

functions of I_p vs $\nu^{1/2}$, the apparent diffusion coefficient of Li⁺ ions for reduction reactions of LTO materials was calculated and is listed in Table 4. Values of D_{Li} are in the range of 10^{-13} to $10^{-11} \text{ cm}^2 \text{ s}^{-1}$. The bare LTO electrode exhibits a diffusion coefficient of 5.4×10^{-13} cm² s⁻¹, which matches well with values of the literature.^{68,69} For example, Deng and coworkers⁶⁸ reported a $D_{\rm Li}$ value of $\sim 5 \times 10^{-12}~{\rm cm^2~s^{-1}}$ for LTO microspheres. The Li-ion diffusion coefficients of RE-doped LTO are higher than that of bare LTO, in agreement with the CV characterizations; not only does the smaller particle size and slight lattice expansion favor lithium paths but the increased electrical properties are beneficial to better kinetics in the doped LTO material. The Eu-LTO electrode exhibits the highest diffusion coefficient $(1.1 \times 10^{-11} \text{ cm}^2 \text{ s}^{-1})$ compared to other RE-doped materials (Table 4), with the same amount of conductive additive loading. This phenomenon is attributed to the larger elementary lattice volume when introducing both Eu3+ and Eu2+ dopants into the spinel structure.

Galvanostatic Charge–Discharge (GCD) Characteristics. Figure 9A shows the initial discharge/charge profiles (potential vs specific capacity curves) of the GCD tests at 1C rate for pristine LTO and RE-LTO electrodes at an ambient temperature. A flat and long potential plateau of around 1.55-1.58 V can be observed for pristine LTO. This feature is characteristic of the two-phase Ti⁴⁺/Ti³⁺ redox reaction corresponding to the Li-ion insertion/extraction in the LTO framework. Initial specific discharge capacities of pristine LTO and RE-doped LTO are in the range of 168-198 mAh g⁻¹ (Table S4), the high capacity being delivered by the Eu-LTO electrode. As expected for the LTO anode materials, the voltage of a $\text{Li}//\text{Li}_{4+x}\text{Ti}_5\text{O}_{12}$ cell changes abruptly at the end of discharge and charge, which is characteristic of a two-phase system. It is well known that during discharge, lithium insertion causes a first-order displacement of the tetrahedrally coordinated Li ions (8a sites) in the Li[Li_{1/3}Ti_{5/3}]O₄ framework into octahedral 16c sites generating the ordered rock-salt phase $\text{Li}_2[\text{Li}_{1/3}\text{Ti}_{5/3}]O_4$ ($\text{Li}_7\text{Ti}_5O_{12}$); thus, in the cutoff potential of 1.0-2.5 V vs Li+/Li, the potential plateau involves the coexistence of the $\text{Li}^{8a}[\text{Li}_{1/3}\text{Ti}_{5/3}]^{16d}[O_4]^{32e}$ and $[\Box]^{8a}[\text{Li}_2]^{16c}[\text{Li}_{1/3}\text{Ti}_{5/3}]^{16d}[O_4]^{32e}$ phases with the simultaneous redox reaction of $\text{Ti}^{4+}/\text{Ti}^{3+}^{65}$ Similar charge—discharge profiles were observed for RE-LTO electrode materials, indicating that RE ions successfully doped in the LTO, in good agreement with voltammetry results. Thus, a $\text{Li}_{4+x}\text{Ti}_5\text{O}_{12}$ spinel anode provides very sharp end-of-charge and end-ofdischarge indicators, which is useful for controlling cell operation and preventing overcharge abuse and overdischarge. The zooming plots of GCD curves in the potential range of 1.52–1.60 V (Figure 9B) show clearly that the cell polarization decreases when RE dopants are inserted in the LTO matrix. The difference between charge and discharge plateau potentials is 24.7 and 15.8 mV for bare LTO and Eu-LTO electrodes, respectively. The obvious difference in the redox potentials can be ascribed to the increased effective conductivity of Ti⁴⁺/Ti³⁺ mixed states and better lithium diffusivity. Figure 9C shows the GCD profiles of the Eu-LTO electrode cycled at various C-rates from 1C to 50C. These charge-discharge curves display the excellent stability of the spinel electrode, revealing a small decrease of the specific discharge capacity at high current densities. Figure 9D-I presents the cyclability curves and the Coulombic efficiency vs cycle number of electrodes tested at 1C rate over 100 cycles for

bare LTO (D), Dy-LTO (E), Ce-LTO (F), Nd-LTO (G), Sm-LTO (H), and Eu-LTO (I). From the data, long-term stability is evident for RE-LTO electrodes. The Li//Eu-LTO cell tested at 1C rate delivers an initial specific discharge capacity of 198 mAh g⁻¹ and displays a capacity retention of 99% and a Coulombic efficiency of 99.92% after 100 cycles. It should be noted that the specific capacity of all RE-LTO electrodes, except Dy-LTO, is higher than the theoretical value for LTO (175 mAh g⁻¹). Such a result has also been evidenced by Cai and co-workers. 41 The additional discharge capacity is not only due to the increasing amount of Ti ions transferred from Ti⁴⁺ to Ti³⁺ by the doping of RE ions for charge balance but also due to the mesoporous nature of RE-doped electrodes, which provides extra space Li+-ion storage. On the other hand, the introduction of foreign ions into the spinel matrix can create a defective mesoporous lattice with oxygen vacancies and Ti³⁺-O²⁻-Ti⁴⁺ pairs, which are features enabling us to improve the storage capacity and rate performance.⁵³ While the bare LTO electrode exhibits a capacity fading of 12 mAh g⁻¹ over 100 cycles or $\Delta Q_d = 0.12$ mAh g⁻¹ per cycle (Figure 9D), a remarkably small drop in specific discharge capacity is observed for RE-doped electrodes with ΔQ_d value almost equal to zero for Eu-LTO after 100 cycles (Figure 9I). This excellent cyclic stability is due to the mesoporous morphology of the electrode material, which can easily accommodate the inserted Li ions and to the decreasing electrode impedance. Using the Nernst-Einstein equation, the electrical conductivity can be estimated from the Li-ion diffusion coefficient

$$\sigma = \frac{nZe^2}{k_{\rm B}T}D_{\rm Li} \tag{9}$$

where $k_{\rm B}$ is the Boltzmann constant, n is the number of carriers in unit volume, Z is the valence of charge carrier, and e is the elementary charge. Combining the Li concentration of 4.37 × 10⁻³ mol cm⁻³ determined from the lattice parameter of 8.331 Å for LTO at room temperature with the D_{Li} values measured (Table 4), σ can be calculated to be approximately 9×10^{-9} and 2×10^{-7} S cm⁻¹ for bare LTO and Eu-LTO, respectively. These values match well with those found for pure LTO and nitrogen-modified LTO materials.

Rate capability tests of the spinel samples were carried out at different discharge rates (1C, 2C, 5C, 10C, 20C, and 50C) in the voltage window of 1.0-2.5 V vs Li+/Li. Results for LTO and RE-LTO electrodes are shown in Figure 9J, and values (with an uncertainty of ± 1 mAh g⁻¹) are listed in Table S4. At a high discharge rate of 50C, Dy-, Ce-, Nd-, Sm-, and Eudoped LTO electrodes exhibit a capacity retention of 68, 69, 69, 71, and 74%, respectively, which are higher than 63% for pristine LTO. The Eu-LTO electrode possesses higher rate capability than bare LTO and other RE-LTO materials. The superior rate performance of Eu-LTO was confirmed by the improvement in specific surface area (mesoporous electrode) and higher apparent diffusion rate of Li ions. The Eu-LTO electrode shows specific discharge capacities of 198, 180, and 148 mAh g^{-1} at 1C, 10C, and 50C current densities (1C = 175 mA g⁻¹ for LTO). Note that after the test at 50 C, the electrode regains its initial capacity when returning to 1C. The specific discharge capacities vs C-rate for the bare LTO and Eu-LTO electrodes tested in the potential range of 1.0-2.5 V vs Li⁺/Li are compared in the modified Peukert plots (Figure 9K). Based on these results, the discharge capacity (Q_d) vs Crate can be expressed using an empirical equation of the form

 $Q_d = Q_o - \alpha \log(C)$, where α is the decay parameter. The best fit (reliability parameter $R^2 = 0.99$) is obtained for Q_0 equals 168 and 202 mAh g⁻¹ and α = 36.8 and 26.8 over the interval 1-50C for bare LTO and Eu-LTO electrodes, respectively. Figure 10 provides a comparison of the electrochemical

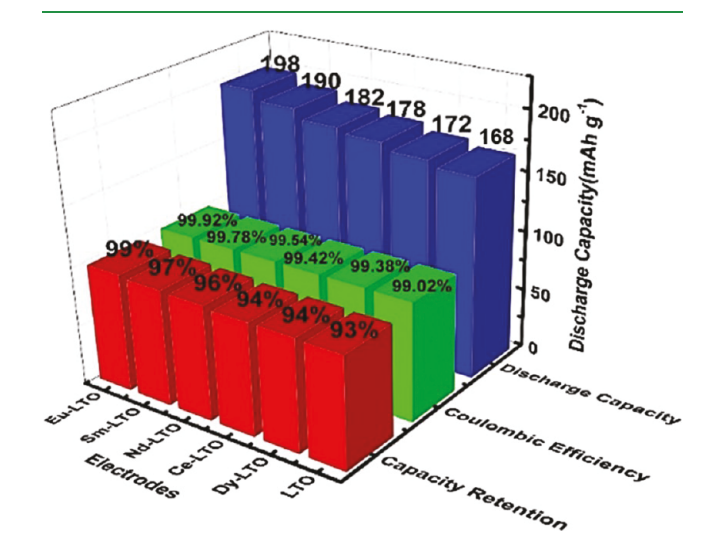


Figure 10. Comparative 3D plot between specific discharge capacity, Coulombic efficiency, and capacity retention of LTO-based electro-

properties of bare LTO and RE-LTO electrodes, i.e., specific discharge capacity, Coulombic efficiency, and capacity retention after cycling over 100 times.

Finally, it seems that the dopant concentration x = 0.1chosen in this work does not affect the change of cell parameters during the charging/discharging process. The change in the cell parameters is almost negligible in this case, which is clearly demonstrated in the Coulombic efficiency and cycling tests. In the present study, equal or more than LTO theoretical capacity values are obtained for all doped electrodes. It should be noted that the specific capacity of all RE-LTO electrodes, except Dy-LTO, is higher than the theoretical value for LTO (175 mAh g⁻¹). Such a result has also been evidenced by Cai and co-workers. ⁴¹ The additional discharge capacity is not only due to the increasing amount of Ti ions transferred from Ti⁴⁺ to Ti³⁺ by doping of RE ions for charge balance but also due to the mesoporous nature of REdoped electrodes, which provides extra space for Li+-ion storage. Moreover, RE doping in the LTO crystal lattice can effectively increase the intrinsic electronic conductivity. The introduction of foreign ions into the spinel matrix can create a defective mesoporous lattice with oxygen vacancies and Ti³⁺-O²⁻-Ti⁴⁺ pairs, which are features that enable us to improve storage capacity and rate performance. On the other hand, LTO or $[Li_3]^{ga}[Li_1\underline{T}i_5]^{16d}[\square]^{16c}[O_{12}]^{32e}$ possesses a spinel structure with the $Fd\overline{3}m$ space group. It is widely accepted that the lithiation mechanism takes 3Li⁺ per formula unit to form $[\, \, \,]^{8a} [Li_1Ti_5]^{16d} [Li_6]^{16c} [\, O_{12}]^{32e}.$ Accordingly, the theoretical capacity of LTO is calculated to be 175 mAh g⁻¹. Its operating potential is in the range of 1.0-2.5 V vs Li⁺/Li. However, the process of Li+ intercalation into the Li₄Ti₅O₁₂ to form Li₇Ti₅O₁₂ only reduces 60% of the Ti⁴⁺ in the crystal to the Ti³⁺. Assuming full utilization of the Ti³⁺/Ti⁴⁺ redox, the $\text{Li}_7\text{Ti}_5\text{O}_{12}$ can take an additional 2 $\text{Li}^{\scriptscriptstyle +}$ to form $\text{Li}_9\text{Ti}_5\text{O}_{12}$ when cycled in the potential range of 0.01-2.5 V vs Li⁺/Li. As also

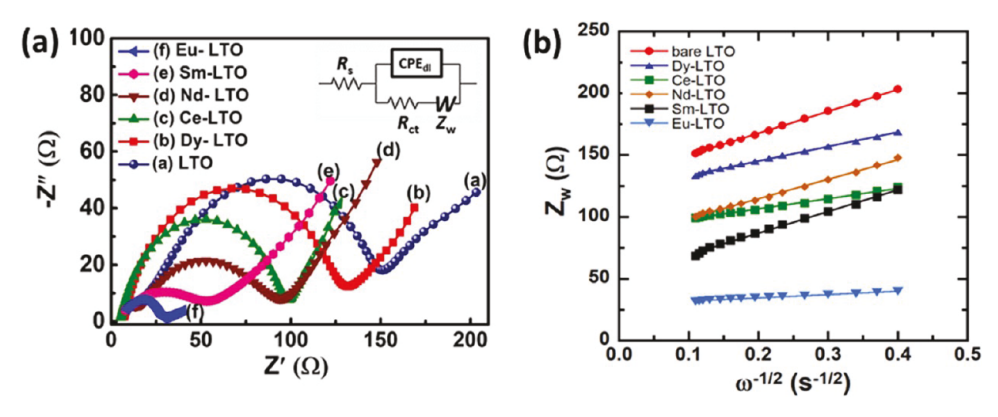


Figure 11. (a) Nyquist plot of bare LTO cell and RE-doped LTO electrodes. The inset shows the equivalent circuit used for EIS fitting. (b) Warburg plots Z' vs $\omega^{-1/2}$.

Table 5. Values of the Randles Circuit Elements Obtained from EIS Analyses of Pristine LTO and RE-LTO Electrodes

electrode	$R_{_{\mathrm{s}}}\left(\Omega\right)$	$R_{\rm ct} \; (\Omega)$	$\mathrm{CPE}_{\mathrm{dl-T}}$	CPE_{dl-p}	$\Omega_{ m w}~(\Omega~{ m s}^{-1/2})$	$D_{{ m Li}^+} ({ m cm}^2 { m s}^{-1})$
LTO	9	139	1.7×10^{-6}	0.58	176	5.5×10^{-14}
Dy-LTO	7	125	7.1×10^{-5}	0.55	117	1.2×10^{-13}
Ce-LTO	7	94	7.5×10^{-5}	0.55	82	2.5×10^{-13}
Nd-LTO	9	82	6.8×10^{-5}	0.56	157	6.9×10^{-14}
Sm-LTO	8	46	6.3×10^{-5}	0.54	175	5.4×10^{-14}
Eu-LTO	8	21	5.8×10^{-5}	0.53	49	7.1×10^{-13}

^aThe uncertainty of the D_{Li} values is estimated to be 4.8%.

evident from the structural point of view, there are additional vacancies to host up to 3 extra Li $^{\rm +}$ at the 8a sites per unit cell to form Li $_9{\rm Ti}_5{\rm O}_{12}$ or even Li $_{10}{\rm Ti}_5{\rm O}_{12}$. Therefore, another strategy is to use more ${\rm Ti}^{3+/}{\rm Ti}^{4+}$ redox sites and be able to absorb 2 Li $^{\rm +}$ ions during the charge-discharge process in order to increase the discharge capacity over the LTO's initial theoretical capacity.

Electrochemical Impedance Spectroscopy (EIS). The EIS measurements were performed to obtain insight into the origin of the different electrochemical performances of RE-LTO materials and corroborate the conductivity of investigated electrodes. The Nyquist plots were carried out over the frequency range from 1 Hz to 1 MHz for the pristine LTO and RE-doped LTO electrodes in the fully charged state for the initial cycle. Experimental results shown in Figures 11a and S6 can be decomposed into three contributions that can be modeled by the Randles equivalent circuit shown in Figure S5. (i) The uncompensated ohmic/solution resistance of the cell (R_s) is determined from the intercept of the high-frequency part of the Nyquist plot with the Z'-axis (horizontal axis), (ii) the charge-transfer impedance (R_{ct}, CPE_{dl}) at the electrode/ electrolyte interface in which CPE_{dl} is the double-layer constant phase element is calculated by a fit of the depressed semicircle in the intermediate-frequency region, and (iii) the Warburg impedance (Z_w) attributed to the diffusion-controlled regime of Li⁺ ions through the bulk electrode corresponds to the EIS response in the low-frequency range, i.e., inclined line. 58 Details of the EIS analyses are given in the Supporting Information. Values of the Randles' circuit elements obtained from the Nyquist curve fitting ($\chi^2 = 4.8$) are listed in Table 5. It is shown that values of R_s are very low $(8 \pm 1 \Omega)$ for both electrodes, which indicates that the ohmic polarization due to the electrolyte is negligible. The $R_{\rm ct}$ value for the bare LTO electrode (139 Ω) is found to be much higher than that of REdoped LTO electrodes. Meanwhile, Eu-LTO has the smallest

 $R_{\rm ct}$ among the samples, implying the highest fast charge-transfer rate. It reveals that the RE doping is effective in increasing electrode conductivity and improving Li⁺ and e⁻ transfer efficiencies, which largely contributes to the rate performance. To account for the improved electrochemical performance of both electrodes, the $D_{\rm Li}$ was evaluated from EIS spectra. Randles plots $Z'vs\omega^{-1/2}$, as well as the Warburg factor $(\sigma_w, {\rm eq~S5})$ representing the mass-controlled process, are illustrated in Figure 11b. The apparent chemical diffusion coefficients can be calculated according to eq 10^{71}

$$D_{\rm Li} = \frac{R^2 T^2}{2A^2 n^4 C_{\rm Li}^2 \sigma^2} \tag{10}$$

Using a concentration of Li⁺ ions of 4.37×10^{-3} mol cm⁻³ in LTO and an effective working area determined by BET measurements, the $D_{\rm Li}$ values are in the range from 5.5×10^{-14} cm² s⁻¹ for bare LTO to 7.1×10^{-13} cm² s⁻¹ for Eu-LTO (Table 5). Eu-LTO has a much faster Li⁺ diffusion coefficient than other RE-doped LTOs, which is in good agreement with the previous structural and morphological analyses. In summary, the europium-modified mesoporous Li₄Ti₅O₁₂ enhances the Li⁺ diffusion coefficient and reduces polarization during the charge-discharge process. It is worth noting that the apparent chemical diffusion coefficients of Li ions in the LTO spinel framework estimated by CV and EIS techniques are not self-consistent, i.e., DLi evaluated from the EIS method is smaller than that from cyclic voltammetry. The applicability of the EIS technique for determining D_{Li} in a two-phase structured electrode is only accurate if the attraction interactions among the insertion sites are moderate. Thus, the difference between D_{Li} values is attributed to the high dependence of D_{Li} on the dE/dx values for the EIS method. The dE/dx values are not accurately determined due to the voltage plateau feature of the two-phase transition reaction $\text{Li}_4\text{Ti}_5\text{O}_{12} \rightarrow \text{Li}_7\text{Ti}_5\text{O}_{12}$. Such discrepancies have also been

reported in the case of LiFePO₄. ⁷² Nevertheless, the same trend is observed for both techniques, *i.e.*, $D_{\rm Li}$ increases in the order LTO < Nd-LTO < Ce-LTO < Nd-LTO < Sm-LTO < Eu-LTO. In Table S5, Li-ion kinetics in RE-doped LTO electrodes are compared with those in the literature. Apparent diffusion coefficients were evaluated from conductivity measurements, electrochemical impedance spectroscopy, and cyclic voltammetry. It is noteworthy that some very high values of $D_{\rm Li}~(\sim 10^{-8}~{\rm cm}^2~{\rm s}^{-1})$ could be due to the use of a geometric electrode surface instead of BET surface area, which is more accurate for a porous electrode.

Comparison with Lanthanide-Doped LTO. On the basis of the aforementioned results and analyses, comparative data of RE-doped LTO samples prepared *via* different methods giving excellent electrochemical performances are compiled in Table 6. It is well understood that three parameters, *i.e.*, morphology,

Table 6. Comparison of the Electrochemical Performance of Ln³+-Doped LTO Electrode Materials^a

ċ	lopant	synthesis ^b	particle size (μm)	specific capacity (mAh g ⁻¹)	cycles	refs
0	.1 Ce	SSR (850 °C/20 h)	1-2	90@10C	50	73
0	.1 Sm	SSR (850 °C/12 h)	0.8	90@5C	100	30
0	.1 Dy	HTT (500 °C/3 h)	0.016 ^c	132@0.2C	5	71
0	.1 Dy	HTT (600 °C/5 h)	0.6×0.3	141@20C	1000	41
0	.15 Ce	SGM (850 °C/12 h)	0.5	143@3C	500	60
0	.1 Ce	SGM (800 °C/18 h)	0.04-0.2	129@20C	600	62
0	.1 Ce	SSR (800 °C/12 h)	~1	136@2C	100	37
0	.01 Eu	BMT (800 °C/7 h)		100@5C	120	32
0	.1 Dy	MCR (850 °C/12 h)	0.049	115@50C	100	this work
0	.1 Ce	MCR (850 °C/12 h)	0.047	122@50C	100	this work
0	.1 Nd	MCR (850 °C/12 h)	0.045	126@50C	100	this work
0	.1 Sm	MCR (850 °C/12 h)	0.044	135@50C	100	this work
0	.1 Eu	MCR (850 °C/12 h)	0.043	148@50C	100	this work
~						

^aTemperature and duration of the final calcination step are given in parentheses. ^bAbbreviations: SSR, solid-state reaction; HTT, hydrothermal technique; SGM, sol–gel method; BMT, ball-milling technique; MCR, mechanochemical reaction. ^cCrystallite size.

particle size, and doping concentration, play significant roles in the electrochemical properties of LTO materials operating as anodes in lithium cells. The differences come not only from the synthesis method itself but also from the temperature and duration of the postannealing treatment. The doping concentration must alter/influence the morphology, particle size, cell parameter, and, consequently, the electrochemical performance of the electrode. Nucleation-growth process being a thermodynamic issue, the difference in the LTO crystallization is due to the change in the enthalpy of formation upon doping. Generally, the enthalpy of formation becomes less negative when increasing the dopant content from undoped. In the SEM images of RE-doped LTO, the grain size has

decreased and particles exhibit a smooth surface. After doping with metal ions, the interconnected particles can be observed. The synthesis procedure is subjected at 850 °C, and the doping can modify the primary particles forming secondary interconnected particles. This interconnected structure can provide a high surface area to accommodate Li⁺ ions during the charge—discharge process, enhancing the discharge capacities, rate capability, and cyclic stability. It can be observed from the TEM images that the grain sizes are also decreased after doping from Dy to Eu. It is attributed to the effect of the respective RE ion with different ionic radii, which can cause internal strain slowing down the growth of particles. Thus, the particle nanoscaling shortens the Li⁺-ion diffusion path and enlarges the electrode/electrolyte contact area involving excellent electrochemical properties.

Among the various forms of RE-doped LTO mesoporous structures including Ce-LTO nanosheets (~40 to 200 nm), ²⁸ Sm-LTO irregular particles (~800 nm) are synthesized by solid-state reaction, ³⁰ Dy-LTO nanoflowers prepared by hydrothermal reaction, ⁴¹ and spindle-shaped Ce-LTO particles. ³⁷ As shown in Table 6, the discharge capacity at high *C*-rates of the RE-doped LTO anodes synthesized *via* mechanochemical reaction evidences obvious advantages (~115, 122, 126, 135, and 148 mAh g⁻¹ at 50C rate for Dy-, Ce-, Nd-, Sm-, and Eu-doped LTO, respectively) over previous values reported for lanthanide-doped LTO electrodes.

SUMMARY AND CONCLUSIONS

In this work, five Li₄Ti₅O₁₂ samples were doped with rare-earth metals (lanthanides) forming $Li_{4-x/3}Ti_{5-2x/3}Ln_xO_{12}$ compounds with similar morphology and particle size whose electrical and electrochemical properties can be easily compared with good accuracy. A facile and effective mechanochemical synthesis with a subsequent calcination at 850 °C for 12 h has been developed to prepare pristine Li₄Ti₅O₁₂ and rare-earth metal (lanthanides)-doped $\text{Li}_{4-x/3}\text{Ti}_{5-2x/3}\text{Ln}_x\text{O}_{12}$ samples. The ball-milling process is an attractive method for the large-scale production of ultrafine, pure, and highly crystalline LTO materials. At a doping level of x = 0.1, structural analyses, i.e., X-ray diffraction and Raman spectroscopy, demonstrate that the LTO spinel crystal phase was retained without any changes in its structure/phase. Results demonstrate that RE doping increases the crystallographic parameters of the LTO framework and improves its structural stability. Raman spectra for as-prepared samples confirmed the formation of phase-pure LTO. The surface morphological studies reveal the homogeneous distribution of primary particles. Thus, the ball-milling method allows the unique mesoporous morphology with a high specific surface area of $\sim 30 \text{ m}^2 \text{ g}^{-1}$ and a submicron particle size in the range of 40-60 nm. The porosity of the RE-LTO samples appeared to be higher than that of bare LTO due to the change of particle interconnection upon RE doping, which can facilitate open channels for Li+-ion storage leading to high electrochemical performance. The RE-doped LTO electrodes delivered specific discharge capacities between 172 and 198 mAh g⁻¹ when cycled at a 1C rate with a potential cutoff of 1.0-2.5 V vs Li⁺/Li. The excess of specific discharge capacity $(Q_d \text{ higher than 168 mAh g}^{-1} \text{ for LTO})$ is attributed to the increasing amount of Ti ions transferred from Ti⁴⁺ to Ti³⁺ by RE doping (charge balance) and to the mesoporous nature of RE-doped electrodes, which provides extra space Li⁺-ion storage. On the other hand, the introduction of foreign ions

into the spinel matrix can create a defective mesoporous lattice with oxygen vacancies and Ti3+O2-Ti4+ pairs, which are features that enable us to improve storage capacity and rate performance. Among all electrodes, Eu-doped LTO showed the best electrochemical performance with a specific discharge capacity of 198 mAh g⁻¹ and a Coulombic efficiency < 99% when tested at a 1C current rate over 100 cycles. This electrode retained 148 mAh g⁻¹ (74% of its initial capacity) at 50C. Furthermore, RE-doped LTO materials, prepared by adding a few percent of lanthanide, have been shown to be used as anodes with high efficiency without the need for expensive carbon coating treatment.

ASSOCIATED CONTENT

Supporting Information

The Supporting Information is available free of charge at https://pubs.acs.org/doi/10.1021/acsami.3c00175.

> Various dopants used to modify the LTO electrodes; schematic representation of the preparation of RE metaldoped $Li_4Ti_5O_{12}$; values of L_c and L_{TEM} for RE-doped LTO samples; binding energy of Ti and Eu elements of bare LTO and Eu-doped LTO compared with literature data; normalized cyclic voltammetry curves for bare and RE-doped LTO electrodes recorded at a scanning rate of 0.5 mV s^{-1} in the potential range of $1.0-2.5 \text{ V vs Li}^+/\text{Li}$; normalized cyclic voltammetry curves for Eu-doped LTO electrodes recorded at various scanning rates $(0.05-10 \text{ mV s}^{-1})$ in the potential range of 1.0-2.5 V vsLi⁺/Li; reversible capacities (mAh g⁻¹) of bare LTO and RE-LTO at various current rates; equivalent circuit model used for simulating the Nyquist plots; Nyquist plots of bare and RE-doped LTO electrodes; particle size distribution of TEM images of pristine LTO and RE-LTO samples; and comparison of Li-ion kinetics in RE-doped LTO electrodes compared to data from the literature (PDF)

(PDF)

AUTHOR INFORMATION

Corresponding Authors

Sang Woo Joo - School of Mechanical and IT Engineering, Yeungnam University, Gyeongsan 38541, Republic of Korea; orcid.org/0000-0001-9102-4224; Email: swjoo@ yu.ac.kr

C. V. Ramana - Center for Advanced Materials Research (CMR), University of Texas at El Paso, El Paso, Texas 79968, United States; Department of Aerospace & Mechanical Engineering, University of Texas at El Paso, El Paso, Texas 79968, United States; o orcid.org/0000-0002-5286-3065; Email: rvchintalapalle@utep.edu

Authors

A. Lakshmi-Narayana – Center for Advanced Materials Research (CMR), University of Texas at El Paso, El Paso, Texas 79968, United States; Department of Aerospace & Mechanical Engineering, University of Texas at El Paso, El Paso, Texas 79968, United States

Merum Dhananjaya - School of Mechanical and IT Engineering, Yeungnam University, Gyeongsan 38541, Republic of Korea

Christian M. Julien – Institut de Minéralogie, de Physique des Matériaux et de Cosmochimie (IMPMC), Sorbonne Université, CNRS-UMR, 75252 Paris, France

Complete contact information is available at: https://pubs.acs.org/10.1021/acsami.3c00175

The authors declare no competing financial interest.

ACKNOWLEDGMENTS

This work was funded by grant NRF-2019R1A5A8080290 of the National Research Foundation of Korea. The authors at UTEP acknowledge, with pleasure, support from the National Science Foundation (NSF) with NSF-PREM grant #DMR-1827745.

REFERENCES

- (1) Miao, Y.; Hynan, P.; von Jouanne, A.; Yokochi, A. Current Li-ion battery technologies in electric vehicles and opportunities for advancements. Energies 2019, 12, No. 1074.
- (2) Wang, J.; Linge, L.; Huimin, H.; Hongfei, H.; Qinghua, G.; Min, H.; Lujie, J.; Henry, A.; Kun, V. T.; Jing, Z.; Stefano, P.; Hongzhen, L. Toward Dendrite-Free Metallic Lithium Anodes: from Structural Design to Optimal Electrochemical Diffusion Kinetics. ACS Nano **2022**, 16, 17729-17760.
- (3) Zaghib, K.; Dontigny, M.; Guerfi, A.; Charest, P.; Rodrigues, I.; Mauger, A.; Julien, C. M. Safe and Fast-Charging Li-Ion Battery with Long Shelf Life For Power Applications. J. Power Sources 2011, 196, 3949-3954.
- (4) Wei, Z.; Zhang, J.; Luo, J.; Zeng, C.; Su, H.; Zhang, J.; Liu, R.; Hu, E.; Liu, Y.; Liu, W.-D.; Chen, Y.; Hu, W.; Xu, Y. Ultra-Fast Non-Equilibrium Synthesis of Cathode Materials for Li-Ion Batteries. Adv. Mater. 2022, 35, No. 2208974.
- (5) Li, Y.; Liu, M.; Feng, X.; Li, Y.; Wu, F.; Bai, Y.; Wu, C. How Can the Electrode Influence the Formation of the Solid Electrolyte Interface? ACS Energy Lett. 2021, 6, 3307-3320.
- (6) Xia, J.; Runhua, G.; Yang, Y.; Zheng, T.; Zhiyuan, H.; Shichao, Z.; Yalan, X.; Puheng, Y.; Xia, L.; Guangmin, Z. ${\rm Ti_nO_{2n-1}/Mxene}$ Hierarchical Bifunctional Catalyst Anchored on Graphene Aerogel Toward Flexible and High-Energy Li-S Batteries. ACS Nano 2022, 16, 19133-19144.
- (7) Koyama, Y.; Chin, T. E.; Rhyner, U.; Holman, R. K.; Hall, S. R.; Chiang, Y. M. Harnessing the Actuation Potential of Solid-State Intercalation Compounds. Adv. Funct. Mater. 2006, 16, 492-498.
- (8) Murphy, D. W.; Cava, R. J.; Zahurak, S. M.; Santoro, A. Ternary Li_xTiO₂ Phases from Insertion Reactions. Solid State Ionics 1983, 9-10, 413-417.
- (9) Gervillié-Mouravieff, C.; Boussard-Plédel, C.; Huang, J.; Leau, C.; Blanquer, L. A.; Yahia, M. B.; Doublet, M. L.; Boles, S. T.; Zhang, X. H.; Adam, J. L.; Tarascon, J. M. Unlocking Cell Chemistry Evolution with Operando Fiber Optic Infrared Spectroscopy in Commercial Na(Li)-Ion Batteries. Nat. Energy 2022, 7, 1157-1169.
- (10) Colbow, K. M.; Dahn, J. R.; Haering, R. R. Structure and Electrochemistry of The Spinel Oxides LiTi₂O₄ and Li_{4/3}Ti_{5/3}O₄. J. Power Sources 1989, 26, 397-402.
- (11) Ge, H.; Hao, T.; Osgood, H.; Zhang, B.; Chen, L.; Cui, L.; Song, X-M.; Ogoke, O.; Wu, G. Advanced Mesoporous Spinel Li₄Ti₅O₁₂/r-GO Composites with Increased Surface Lithium Storage Capability for High-Power Lithium-Ion Batteries. ACS Appl. Mater. Interfaces 2016, 8, 9162-9169.
- (12) Wang, L.; Zhang, Z.; Cheng, Y.; Zhang, Y.; Liu, W.; Su, J.; Liu, N.; Gao, Y. Revealing the Phase-Transition Dynamics and Mechanism in a Spinel Li₄Ti₅O₁₂ Anode Material Through in Situ Electron Microscopy. ACS Appl. Mater. Interfaces 2020, 12, 20874-20881.
- (13) Sugiyama, J.; Umegaki, I.; Uyama, T.; McFadden, R. M.; Shiraki, S.; Hitosugi, T.; Salman, Z.; Saadanoui, H.; Morris, G. D.; MacFarlane, W. A.; Kieft, R. K. Lithium Diffusion in Spinel Li₄Ti₅O₁₂

- and $LiTi_2O_4$ Films Detected with ⁸Li B-NMR. *Phys. Rev. B* **2017**, *96*, No. 094402.
- (14) Ohzuku, T.; Ueda, A.; Yamamoto, N. Zero-Strain Insertion Material of $\text{Li}[\text{Li}_{1/3}\text{Ti}_{5/3}]\text{O}_4$ for Rechargeable Lithium Cells. *J. Electrochem. Soc.* **1995**, *142*, 1431–1435.
- (15) Sun, C.; Ji, X.; Weng, S.; Li, R.; Huang, X.; Zhu, C.; Xiao, X.; Deng, T.; Fan, L.; Chen, L.; Wang, X.; Wang, C.; Fan, X. 50C Fast-Charge Li-Ion Batteries Using a Graphite Anode. *Adv. Mater.* 2022, 34, No. 2206020.
- (16) Zaghib, K.; Simoneau, M.; Armand, M.; Gauthier, M. Electrochemical Study of $\text{Li}_4\text{Ti}_5\text{O}_{12}$ as Negative Electrode for Li-Ion Polymer Rechargeable Batteries. *J. Power Sources* **1999**, 81-82, 300-305.
- (17) Wolfenstine, J.; Lee, U.; Allen, J. L. Electrical Conductivity and Rate-Capability of Li₄Ti₅O₁₂ as a Function of Heat-Treatment Atmosphere. *J. Power Sources* **2006**, *154*, 287–289.
- (18) Yan, H.; Zhang, D.; Qilu; Duo, X.; Sheng, X. A Review of Spinel Lithium Titanate (Li₄Ti₅O₁₂) as Electrode Material for Advanced Energy Storage Devices. *Ceram. Int.* **2021**, *47*, 5870–5895.
- (19) Jung, H.-G.; Myung, S.-T.; Yoon, C. S.; Son, S.-B.; Oh, K. H.; Amine, K.; Scrosati, B.; Sun, Y.-K. Microscale Spherical Carbon-Coated Li₄Ti₅O₁₂ as Ultra-High Power Anode Material for Lithium Batteries. *Energy Environ. Sci.* **2011**, *4*, 1345–1351.
- (20) Ni, H. F.; Fan, L. Z. Nano-Li₄Ti₅O₁₂ Anchored on Carbon Nanotubes by Liquid Phase Deposition as Anode Material for High Rate Lithium-Ion Batteries. *J. Power Sources* **2012**, *214*, 195–199.
- (21) Bae, S.; Nam, I.; Park, S.; Yoo, Y. G.; Yu, S.; Lee, J. M.; Han, J. W.; Yi, J. Interfacial Adsorption and Redox Coupling of $\text{Li}_4\text{Ti}_5\text{O}_{12}$ With Nanographene for High-Rate Lithium Storage. *ACS Appl. Mater. Interfaces* **2015**, 7, 16565–16572.
- (22) Wang, L.; Zhang, Y.; Guo, H.; Li, J.; Stach, E. A.; Tong, X.; Takeuchi, E. S.; Takeuchi, K. J.; Liu, P.; Marschilok, A. C.; Wong, S. S. Structural and Electrochemical Characteristics of Ca-Doped 'Flower-Like' Li₄Ti₅O₁₂ Motifs as High-Rate Anode Materials for Lithium-Ion Batteries. *Chem. Mater.* **2018**, *30*, *671*–684.
- (23) Zhao, B.; Ran, R.; Liu, M.; Shao, Z. A Comprehensive Review of Li₄Ti₅O₁₂ -Based Electrodes for Lithium-Ion Batteries: The Latest Advancements and Future Perspectives. *Mater. Sci. Eng. R* **2015**, *98*, 1–71.
- (24) Ouyang, C. Y.; Zhong, Z. Y.; Lei, M. S. Ab Initio Studies of Structural and Electronic Properties of Li₄Ti₅O₁₂ Spinel. *Electrochem. Commun.* **2007**, *9*, 1107–1112.
- (25) Lin, C. F.; Fan, X. Y.; Xin, Y. L.; Cheng, F. Q.; Lai, M. O.; Zhou, H. H.; Lu, L. Li₄Ti₅O₁₂-Based Anode Materials with Low Working Potentials, High Rate Capabilities and High Cyclability for High-Power Lithium-Ion Batteries: A Synergistic Effect of Doping, Incorporating A Conductive Phase and Reducing the Particle Size. J. Mater. Chem. A 2014, 2, 9982–9993.
- (26) Bai, Y.-J.; Gong, C.; Qi, Y.-X.; Lun, N.; Feng, J. Excellent Long-Term Cycling Stability of La-Doped $\text{Li}_4\text{Ti}_5\text{O}_{12}$ Anode Material at High Current Rates. *J. Mater. Chem.* **2012**, 22, 19054–19060.
- (27) Wu, Z. L.; Xu, G. B.; Wei, X. L.; Yang, L. W. Highly-Crystalline Lanthanide Doped and Carbon Encapsulated Li₄Ti₅O₁₂ Nanosheets as an Anode Material for Sodium Ion Batteries with Superior Electrochemical Performance. *Electrochim. Acta* **2016**, 207, 275–283.
- (28) Feng, J.; Wang, Y. Ce-Doped Li₄Ti₅O₁₂/C Nanoparticles Embedded in Multiwalled Carbon Nanotube Network as a High-Rate and Long Cycle-Life Anode for Lithium-Ion Batteries Application. *Ceram. Int.* **2016**, *42*, 19172–19178.
- (29) Qin, M.; Li, Y.; Lv, X.-J. Preparation of Ce- and La-Doped Li₄Ti₅O₁₂ Nanosheets and Their Electrochemical Performance in Li Half Cell and Li₄Ti₅O₁₂/Lifepo₄ Full Cell Batteries. *Nanomaterials* **2017**, *7*, No. 150.
- (30) Li, Z.; Li, J.; Zhao, Y.; Yang, K.; Gao, F.; Li, X. Structure and Electrochemical Properties of Sm Doped ${\rm Li_4Ti_5O_{12}}$ as Anode Material for Lithium-Ion Batteries. *RSC Adv.* **2016**, *6*, 15492–15500.
- (31) Michalska, M.; Lemanski, K.; Ptak, M.; Roguska, A.; Chernyayeva, O.; Zurek, P.; Sikora, A.; Gołębiewski, P.; Szysiak, A.; Malinowska, A.; Małecka, M. Effects of Eu³⁺ Ions Doping on

- Physicochemical Properties of Spinel-Structured Lithium-Titanium Oxide $(Li_4Ti_5O_{12})$ as an Efficient Photoluminescent Material. *Mater. Res. Bull.* **2021**, 134, No. 111084.
- (32) Cai, Y.; Huang, Y.; Jia, W.; Wang, X.; Guo, Y.; Jia, D.; Sun, Z.; Pang, W.; Guo, Z. Super High-Rate, Long Cycle Life of Europium-Modified, Carbon-Coated, Hierarchical Mesoporous Lithium-Titanate Anode Materials for Lithium Ion Batteries. *J. Mater. Chem. A* **2016**, *4*, 9949–9957.
- (33) Li, Y.; Wang, Z.; Zhao, D.; Zhang, L. Gd Doped Single-Crystalline Li₄Ti₅O₁₂/TiO₂ Nanosheets Composites as Superior Anode Material in Lithium Ion Batteries. *Electrochim. Acta* **2015**, 182, 368–375.
- (34) Xu, G. B.; Yang, L. W.; We, X. L.; Ding, J. W.; Zhong, J. X.; Chu, P. K. Highly-Crystalline Ultrathin Gadolinium Doped and Carbon-Coated $\rm Li_4Ti_5O_{12}$ Nanosheets for Enhanced Lithium Storage. *J. Power Sources* **2015**, 295, 305–313.
- (35) Ding, K.; Zhao, J.; Zhao, J.; Zhao, Y.; Chen, Y.; Zhang, Y.; Wei, B.; Wang, L.; He, X. Preparation and Characterization of Dy-Doped Lithium Titanate ($\text{Li}_4\text{Ti}_5\text{O}_{12}$). *Int. J. Electrochem. Sci.* **2016**, *11*, 446–458
- (36) Yang, S.-Y.; Yuan, J.; Zhu, Y.-R.; Yi, T.-F.; Xie, Y. Structure and Electrochemical Properties of Sc³⁺-Doped Li₄Ti₅O₁₂ as Anode Materials for Lithium-Ion Battery. *Ceram. Int.* **2015**, *41*, 7073–7079.
- (37) Zhou, T. P.; Feng, X. Y.; Guo, X.; Wu, W. W.; Cheng, S.; Xiang, H. F. Solid-State Synthesis and Electrochemical Performance of Ce-Doped Li₄Ti₅O₁₂ Anode Materials for Lithium-Ion Batteries. *Electrochim. Acta* **2015**, *174*, 369–375.
- (38) Rodriguez-Carjaval, J. Recent Developments of the Program FULLPROF. Commission on Powder Diffraction (Iucr). Newsletter 26, 2001; pp 12–19.
- (39) Jiang, Y.-M.; Wang, K.-X.; Zhang, H.-J.; Wang, J.-F.; Chen, J.-S. Hierarchical Li₄Ti₅O₁₂/TiO₂ Composite Tubes with Regular Structural Imperfection for Lithium Ion Storage. *Sci. Rep.* **2013**, *3*, No. 3490.
- (40) Shannon, R. D. Revised Effective Ionic Radii and Systematic Studies of Interactomic Distances in Halides and Chalcogenides. *Acta Crystallogr., Sect. A: Cryst. Phys., Diffr., Theor. Gen. Crystallogr.* **1976**, 32, 751–767.
- (41) Cai, Y.; Huang, Y.; Jia, W.; Zhang, Y.; Wang, X.; Guo, Y.; Jia, D.; Pang, W.; Guo, Z.; Wang, L. Two-Dimensional Dysprosium-Modified Bamboo-Slip-Like Lithium Titanate with High-Rate Capability and Long Cycle Life for Lithium-Ion Batteries. *J. Mater. Chem. A* **2016**, *4*, 17782–17790.
- (42) Calos, N. J.; Forrester, J. S.; Schaffer, G. B. A Crystallographic Contribution to the Mechanism Mechanically Induced Solid State Reaction. *J. Solid State Chem.* **1996**, *122*, 273–280.
- (43) Lin, C. F.; Lai, M. O.; Lu, L.; Zhou, H. H.; Xin, Y. L. Structure and High Rate Performance of Ni²⁺ Doped Li₄Ti₅O₁₂ for Lithium Ion Battery. *J. Power Sources* **2013**, 244, 272–279.
- (44) Mote, V. D.; Purushotham, Y.; Dole, B. N. Williamson-Hall Analysis in Estimation of Lattice Strain in Nanometer-Sized ZnO Particles. *J. Theor. Appl. Phys.* **2012**, *6*, No. 6.
- (45) Li, T.; Chang, K.; Hashem, A. M.; Abdel-Ghany, A. E.; El-Tawil, R. S.; Wang, H.; El-Mounayri, H.; Andres Tovar, A.; Zhu, L.; Julien, C. M. Structural and Electrochemical Properties of the High Ni Content Spinel LiNiMnO₄. *Electrochem* **2021**, *2*, 95–117.
- (46) Ansari, S. M.; Sinha, B. B.; Phase, D.; Sen, D.; Sastry, P. U.; Kolekar, Y. D.; Ramana, C. V. Particle Size, Morphology, and Chemical Composition Controlled CoFe₂O₄ Nanoparticles with Tunable Magnetic Properties via Oleic Acid Based Solvothermal Synthesis for Application in Electronic Devices. *ACS Appl. Nano Mater.* **2019**, *2*, 1828–1843.
- (47) Ramana, C. V.; Ait-Salah, A.; Utsunomiya, S.; Morhange, J. F.; Mauger, A.; Gendron, F.; Julien, C. M. Spectroscopic and chemical imaging analysis of lithium iron triphosphate. *J. Phys. Chem. C* **2007**, *111*, 1049–1054.
- (48) Ramana, C. V.; Ait-Salah, A.; Utsunomiya, S.; Mauger, A.; Gendron, F.; Julien, C. M. Novel lithium iron pyrophosphate

- (LiFe_{1.5} P_2O_7) as a positive electrode for Li-ion batteries. *Chem. Mater.* **2007**, *19*, 5319–5324.
- (49) Julien, C. M.; Massot, M. Raman Spectroscopic Studies of Lithium Manganates with Spinel Structure. *J. Phys.: Condens. Matter* **2003**, *15*, 3151–3162.
- (50) Julien, C. M.; Massot, M.; Zaghib, K. Structural Studies of $Li_{4/3}Me_{5/3}O_4$ (Me=Ti, Mn) Electrode Materials: Local Structure and Electrochemical Aspects. *J. Power Sources* **2004**, *136*, 72–79.
- (51) Mukai, K.; Kato, Y. Role of Oxide Ions in Thermally Activated Lithium Diffusion of $\text{Li}[\text{Li}_{1/3}\text{Ti}_{5/3}]\text{O}_4$: X-Ray Diffraction Measurements and Raman Spectroscopy. *J. Phys. Chem. C* **2015**, *119*, 10273–10281.
- (52) Xiaobing, L.; Holland, J.; Burgess, S.; Bhadare, S.; Yamaguchi, S.; Birtwistle, D.; Statham, P.; Rowlands, N. Detection of Lithium X-rays by EDS. *Microsc. Microanal.* **2013**, *19*, 1136–1137.
- (53) Song, H.; Yun, S. W.; Chun, H. H.; Kim, M. G.; Chung, K. Y.; Kim, H. S.; Cho, B. W.; Kim, Y. T. Anomalous Decrease in Structural Disorder Due to Charge Redistribution in Cr-Doped Li₄Ti₅O₁₂ Negative-Electrode Materials for High-Rate Li-Ion Batteries. *Energy Environ. Sci.* **2012**, *5*, 9903–9913.
- (54) Chen, X.; Guan, X.; Li, L.; Li, G. Defective Mesoporous Li₄Ti₅O_{12-y}: An Advanced Anode Material with Anomalous Capacity and Cycling Stability at a High Rate of 20C. *J. Power Sources* **2012**, 210, 297–302.
- (55) Sun, X.; Radovanovic, P. V.; Cui, B. Advances in Spinel Li₄Ti₅O₁₂ Anode Materials for Lithium-Ion Batteries. *New J. Chem.* **2015**, 39, 38–63.
- (56) Bardestani, R.; Patience, G. S.; Kaliaguine, S. Experimental Methods in Chemical Engineering: Specific Surface Area and Pore Size Distribution Measurements BET, BJH, and DFT. *Can. J. Chem. Eng.* **2019**, *97*, 2781–2791.
- (57) Ilican, S. Effect of Na Doping on the Microstructures and Optical Properties of ZnO Nanorods. *J. Alloys Compd.* **2013**, 553, 225–232.
- (58) Diebold, U.; Madey, T. E. TiO₂ by XPS. Surf. Sci. Spectra **1996**, 4, 227–231.
- (59) Zhang, P.; Huang, Y.; Jia, W.; Cai, Y.; Wang, X.; Guo, Y.; Jia, D.; Sun, Z.; Guo, Z. Improved Rate Capability and Cycling Stability of Novel Terbium-Doped Lithium Titanate for Lithium-Ion Batteries. *Electrochim. Acta* **2016**, 210, 935–941.
- (60) Zhang, Q.; Liu, Y.; Lu, H.; Tang, D.; Ouyang, C.; Zhang, L. Ce^{3+} -Doped $Li_4Ti_5O_{12}$ with CeO_2 Surface Modification by a Sol-Gel Method for High-Performance Lithium-Ion Batteries. *Electrochim. Acta* **2016**, *189*, 147–157.
- (61) Zhang, Q. Y.; Zhang, C. L.; Li, B.; Jiang, D. D.; Kang, S. F.; Li, X.; Wang, Y. G. Preparation and Electrochemical Properties of Ca-Doped Li₄Ti₅O₁₂ as Anode Materials in Lithium-Ion Battery. *Electrochim. Acta* **2013**, *107*, 139–146.
- (62) El Ouatani, L.; Dedryvère, R.; Siret, C.; Biensan, P.; Gonbeau, D. Effect of Vinylene Carbonate Additive in Li-Ion Batteries: Comparison of LiCoO₂/C, LiFePO₄/C, and LiCoO₂/Li₄Ti₅O₁₂ Systems. *J. Electrochem. Soc.* **2009**, *156*, No. A468.
- (63) Zhao, F.; Sun, H. L.; Gao, S.; Su, G. Synthesis and Size Dependent Magnetic Properties Of Mono Disperse EuS Nanocrystals. *Small* **2006**, *2*, 244–248.
- (64) Le, F.; Wang, L.; Jia, W.; Jia, D.; Bao, S. Synthesis and Photoluminescence of Eu^{2+} by Co-Doping Eu^{3+} and Cl^- in $Sr_2P_2O_7$ Under Air Atmosphere. *J. Alloys Compd.* **2012**, *512*, 323–327.
- (65) Sun, X.; Radovanovic, P. V.; Cui, B. Advances in Spinel Li₄Ti₅O₁₂ Anode Materials for Lithium-Ion Batteries. *New J. Chem.* **2015**, *39*, 38–63.
- (66) Zhang, K.; Park, M.; Zhou, L.; Lee, G.-H.; Li, W.; Kang, Y.-M.; Chen, J. Urchin-Like CoSe₂ as a High-Performance Anode Material for Sodium-Ion Batteries. *Adv. Funct. Mater.* **2016**, *26*, 6728–6735.
- (67) Deng, S.; Li, J. W.; Sun, S.; Wang, H.; Liu, J.; Yan, H. Synthesis and Electrochemical Properties of Li₄Ti₅O₁₂ Spheres and Its Application for Hybrid Supercapacitors. *Electrochim. Acta* **2014**, *146*, 37–43.

- (68) Krajewski, M.; Hamankiewicz, B.; Michalska, M.; Andrzejczuk, M.; Lipinska, L.; Czerwinski, A. Electrochemical Properties of Lithium Titanium Oxide, Modified with Ag-Cu Particles, as a Negative Electrode for Lithium-Ion Batteries. RSC Adv. 2017, 7, 52151–52164.
- (69) Li, X.; Lin, H.; Cui, W.; Xiao, Q.; Zhao, J. Fast Solution-Combustion Synthesis of Nitrogen-Modified Li₄Ti₅O₁₂ Nanomaterials with Improved Electrochemical Performance. *ACS Appl. Mater. Interfaces* **2014**, *6*, 7895–7901.
- (70) Bard, A. J.; Faulkner, L. R. Electrochemical Methods: Fundamentals and Applications; Wiley & Sons, Inc.: New York, NY, USA, 2001; pp 226–260.
- (71) Salvatore, K. L.; Vila, M. N.; Renderos, G.; Li, W.; Housel, L. M.; Tong, X.; McGuire, S. C.; Gan, J.; Paltis, A.; Lee, K.; Takeuchi, K. J.; Marschilok, A. C.; Takeuchi, E. S.; Wong, S. S. Probing the Physicochemical Behavior of Variously Doped Li₄Ti₅O₁₂ Nanoflowers. *ACS Phys. Chem Au* **2022**, *2*, 331–345.
- (72) Tang, K.; Yu, X.; Sun, J.; Li, H.; Huang, X. Kinetic Analysis on LiFePO₄ Thin Films by CV, GITT, and EIS. *Electrochim. Acta* **2011**, *56*, 4869–4875.
- (73) Yi, T.-F.; Wu, J.-Z.; Li, M.; Zhu, Y.-R.; Xie, Y.; Zhu, R.-S. Enhanced Fast Charge–Discharge Performance of Li₄Ti₅O₁₂ as Anode Materials for Lithium-Ion Batteries by Ce and CeO₂ Modification Using a Facile Method. *RSC Adv.* **2015**, *5*, 37367–37376.

TRecommended by ACS

Enhanced Electrochemical Performance of the $LiNi_{0.5}Mn_{1.5}O_4$ Cathode Material by the Construction of Uniform Lithium Silicate Nanoshells

Yuan Zhang, Guangchuan Liang, et al.

DECEMBER 23, 2022

ACS APPLIED MATERIALS & INTERFACES

READ 🗹

Preparation of SOFC Anodes at Lower Temperature with Boosted Electrochemical Performance

Zhishan Li, Yifei Sun, et al.

MARCH 07, 2023

ACS APPLIED ENERGY MATERIALS

READ 🗹

Revealing the Ultrahigh Rate Performance of the La and Ce Co-doping ${\bf LiFePO_4}$ Composite

Baofeng Zhang, Youlong Xu, et al.

NOVEMBER 16, 2022

ACS APPLIED ENERGY MATERIALS

READ 🗹

Depth-Dependent Understanding of Cathode Electrolyte Interphase (CEI) on the Layered Li-Ion Cathodes Operated at Extreme High Temperature

Sudhan Nagarajan, Leela Mohana Reddy Arava, et al.

MAY 03, 2022

CHEMISTRY OF MATERIALS

READ 🗹

Get More Suggestions >